2004

Non-homogeneous atmospheric modeling using MM5 and MODTRAN

David A. Bennett
San Jose State University

NOTE TO USERS

NON-HOMOGENEOUS ATMOSPHERIC MODELING USING MM5 AND MODTRAN

A Thesis Presented to

The Faculty of the Department of Meteorology

San Jose State University

In Partial Fulfillment

Of the Requirements for the Degree

Master of Science

By

David A. Bennett

August 2004

INFORMATION TO USERS

The quality of this reproduction is dependent upon the quality of the copy submitted. Broken or indistinct print, colored or poor quality illustrations and photographs, print bleed-through, substandard margins, and improper alignment can adversely affect reproduction.

In the unlikely event that the author did not send a complete manuscript and there are missing pages, these will be noted. Also, if unauthorized copyright material had to be removed, a note will indicate the deletion.

ProQuest Information and Learning Company
300 North Zeeb Road
P.O. Box 1346
Ann Arbor, MI 48106-1346

APPROVED FOR THE DEPARTMENT OF METEOROLOGY

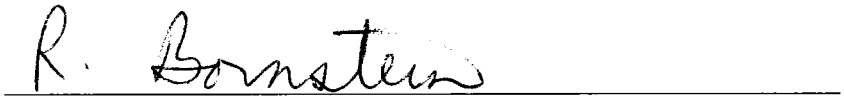

Prof. Robert Bornstein

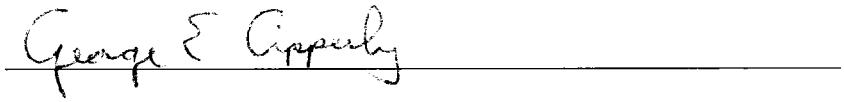

Dr. George E. Cipperly (Lockheed Martin Integrated Systems & Solutions)

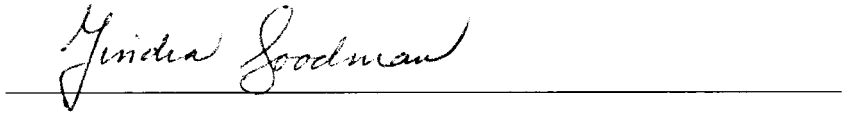

Prof. Jindra Goodman

APPROVED FOR THE UNIVERSITY

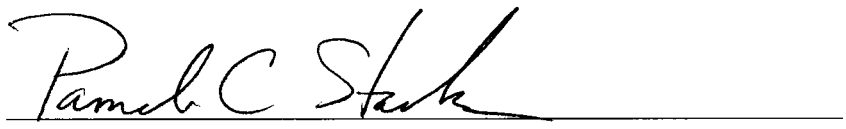

ABSTRACT

NON-HOMOGENEOUS ATMOSPHERIC MODELING
USING MM5 AND MODTRAN

By David A. Bennett

Future remote sensing satellite missions exploring the Earth's surface and atmosphere will feature advanced optical imaging instruments and complex data processing algorithms. Given the nature of these systems, a thorough evaluation of the performance of both the sensor and algorithms will have to be performed before launch. This evaluation can be performed by use of realistic and accurate simulations of the imaging system. A scene simulation system was thus developed using the MM5 mesoscale modeling system, coupled with the MODTRAN radiative transfer model, which addressed the non-homogeneous nature of atmospheric radiative transfer. Simulated VIIRS SDR results are compared to observed MODIS SDR values to demonstrate the accuracy of the radiative transport calculations performed with this modeling system. Results showed that simulated VIIRS data was in excellent agreement when compared to observed MODIS data, and the modeling system demonstrated that it effectively models first level phenomenology for extended complex scenes.

Acknowledgements

There are many people, including family, friends, and colleagues, to whom I am gratefully thankful. I would first like to thank my family for their emotional (and financial) support since I began college, and for backing me in whatever choices I made over the years. I would like to thank my friends who supported me with encouragement while I studied and worked on this project. I would like to thank my wife Suzanne, who has provided me with unwavering support and companionship since the day we met.

There are many colleagues who have provided me with endless technical insight and support over the years. I would like to first thank Phillip Topping, Dr. Keith Hutchison, and Dave Paul for hiring me into the CREST Lab as a graduate student, and eventually bringing me on full time to work on the NPOESS proposal. I would also like to thank Jack Twomey for his programming expertise, James Locke for his engineering support and traveling partnership, and Scott Wilcox and Dr. George Cipperly for the great work experience while building this modeling system, both technically and personally. I would like to further thank George for agreeing to review this paper and for his valuable insight and expertise in atmospheric radiative transfer.

I would like to the Meteorology department at San Jose State University for providing me with a great education, and for putting up with me, and especially to my advisor, Prof. Bob Bornstein who offered me a great career opportunity to come to SJSU and work at Lockheed Martin. I would like to thank you for always having an open door policy, being available for conversation, for the many revisions of this paper, and for your valuable technical insight to numerical modeling.

Table of Contents

List of Tables

List of Figures

1. Introduction

The basic physical problem to be solved in satellite meteorology is "what temperature and trace gas concentration could have produced a set of observed radiances?" This problem is called the inverse or retrieval problem. The opposite problem, called the forward problem, is to calculate outgoing radiances given a set of temperature and trace gas profiles (Kidder and Vonder Harr 1995). With this in mind, the basic concept of a "round trip simulation" is to start with atmospheric state variables (profiles of temperature, moisture, and gaseous absorber properties) and surface properties that will provide the *a-priori* truth. This truth-vector is then used as input to a radiative transfer model (a.k.a. forward model) to calculate outgoing radiances at the wavelengths of interest. Outgoing radiances values are then used as input to a retrieval algorithm to extract the geophysical value of interest. This geophysical value (e.g., temperature profile) is then compared to the input atmospheric state truth-vector to evaluate algorithm performance.

Simulation of sensor-data is complicated because entrance aperture radiances (EAR) must have noise and estimated calibration error added to them, and scenes with spatial structure must be degraded by modulation transfer function (MTF) loss effects and by the effects of sampling with finite sized detectors. The retrieval problem is further complicated as the solution to the radiative transfer equation may not be unique. This is particularly true of multi-spectral sensors systems, but even more so of hyper-spectral sensor systems. Different profiles of moisture, temperature, and trace gases can thus give the same radiance values.

Once a sensor has been designed and an algorithm developed, the difficult tasks of testing and evaluating algorithm performance must be addressed, historically by use of test images that have been extensively ground truthed. The limitation of this approach is the availability of well-characterized test datasets, e.g., a dataset may not contain the atmospheric phenomenon of interest, such as cirrus clouds over snow. Another limitation is the lack of diversity in available datasets, which limits the ability to test algorithms over a wide range of conditions (DIRS 2004).

Use of synthetic datasets thus provides per-pixel ground truth that allows algorithm performance to be evaluated at every pixel, rather than only for a few targets and atmospheric paths for which ground truth data have been collected. Synthetic data can be generated at a significant cost savings, when compared to those from extensive field collection campaigns. At no point in time, however, should it be expected that state-of-the-art image generation modeling systems be robust enough to be the only testing tool. It is more appropriate for synthetic imagery to provide a valuable complement to real imagery or to be used as a possible surrogate when real data are not available (DIRS 2004). When a synthetic image generation model is utilized, the user can create a large set of test images that feature variations in scene type, time of day, and atmospheric conditions to evaluate algorithms under more conditions.

Many modeling techniques exist (Berk et al. 2001, Posselt 2003, Schott et al. 1992, Richtsmeier 2001) to generate simulated radiance values as seen from satellite or airborne sensors. They range in complexity from sophisticated ray tracing codes that use surface scenes created with 3-D computer aided design (CAD) tools coupled with radiative trans-

fer models to single pixel, single profile systems. One simple standard approach to estimate the radiance at the top of the atmosphere (TOA) is by use of a forward model, such as MODerate resolution atmospheric TRANsmission (MODTRAN) (Berk et al. 1989) or Fast Atmospheric Signature CODE (FASCODE) (Smith et al. 1978). These models calculate the following radiance fluxes transmitted to the sensor: (a) reflected direct (solar and thermal) from the target, (b) reflected diffuse downwelling from the target, (c) solar and thermal radiances scattered and/or emitted along the upward path, and (d) thermal radiance emitted by the target.

With MODTRAN, one of six built in generic atmospheric profiles can be selected to describe atmospheric characteristics along a single path. These profiles, principally derived from years of RAOB observations averaged over time and space, include: tropical, mid-latitude summer, mid-latitude winter, sub-arctic summer, sub-artic winter, and the 1976 U.S. Standard Atmosphere. Strengths of this approach are that the profiles are widely used, and that they can provide accurate and useful radiance and transmission datasets for subsequent algorithm development when combined with the scattering; viewing and solar geometry variations; surface characteristics; and cloud and aerosol options within MODTRAN and FASCODE.

One weakness of this approach, however, is that the atmosphere is treated as horizontally homogeneous. Thus, during the forward calculation, the radiance from the sun to the target, the downwelling radiance from throughout the hemispheric surround, and the radiance from the target to the sensor are all calculated for the same vertical distribution of meteorological parameters (although varying zenith angles are taken into account). It

also means that all targets within an image are thus modeled as having the same meteorological profiles along there various lines-of-sight. Another limitation is that temperature and moisture profiles tend to vary smoothly with altitude, and thus do not represent atmospheric profiles typical of active weather regions.

Another approach to the simulation of satellite radiance data involves use of a profile from an actual observation, such as from a RAOB or rocketsonde. These profiles are then used as input to a forward model to estimate TOA radiance values for a given location and time. A benefit of this approach is that moisture and temperature profiles represent the atmosphere over a range of realistic conditions. With a satellite observation coincident with a profile, simulated and observed radiance values can be compared. The limitation to this approach, however, is similar to the use of standard profiles, as the atmosphere is still treated as horizontally homogeneous during the forward calculation.

Some modeling systems use 3-D CAD models of buildings, automobiles, and vegetation, along with their associated spectral and thermodynamic properties. Resulting 3-D scenes are used in conjunction with a sensor model to define viewing geometry and with ray tracing codes coupled with radiative transfer models (e.g., MODTRAN) to generate synthetic scenes with high spectral and spatial fidelity. The most mature and widely used of these systems is Digital Image Remote Sensing Image Generator (DIRSIG) (Schott et al. 1992), developed at the Rochester Institute of Technology (RIT). It is an integrated collection of independent first principles-based sub-models that work together to produce radiance field images with high radiometric fidelity in the 0.3-20 μm region. Its modular design creates a high degree of flexibility and interchangeability, as well as the capability

to diagnose and improve the system by the isolation and analysis of each sub-model (DIRS 2004). Modeling systems like DIRSIG generate scenes that cover an area ranging from several hundred meters to a few kilometers, with a ground sampling distance (GSD) down to a few inches.

All the modeling techniques previously mentioned, however, treats the geophysical properties of the atmosphere as slab symmetric. Sensors on weather and climate satellites, such as the visible infra-red imaging radiometer suite (VIIRS) on the national polar-orbiting operational environmental satellite system (NPOESS), however, can have field of views greater than 3000 km. To accurately model radiances reaching such sensors, the non-homogeneous nature of the atmosphere must be taken into account. The 3-D nature of atmospheric radiative transfer is an important phenomenon, and until recently it has not been directly addressed in the above image simulation systems.

One radiative transport modeling system under development to address atmospheric horizontal in-homogeneity is MOD3D (Berk et al. 2001), a rapid and accurate algorithm for applications to 3-D simulations. It couples optical property databases generated by the MODTRAN4 Correlated-k (CK) band model-algorithm. The CK algorithm compensates for the non-Beer's Law behavior of the band model underlying MODTRAN, resulting in a proper combination of effects along the downwelling and upwelling paths. Full 3-D spatial effects are modeled by scaling and interpolating optical data to local conditions, and the model has been integrated into the Joint Modeling and Simulation System (JMASS) for calculation of path transmittances, thermal emission, and single scatter solar radiation (Berk et al. 2001). The JMASS program is responsible for devel-

opment of a standard digital modeling and simulation architecture and tool set, as well as of a Modeling and Simulation Reuse Library (MSRL) to support analysis, development, acquisition, testing, and evaluation of weapons systems.

Another modeling system is under development by Spectral Sciences Inc. (SSI) (Richtsmeier et al. 2001). Its high fidelity hyperspectral image (HSI) simulation software is based on a Direct Simulation Monte Carlo (DMSC) approach for modeling 3-D atmospheric radiative transport and spatially inhomogeneous surfaces, including surface bi-directional reflective distribution function (BRDF) effects. The system includes both land and ocean surfaces, 3-D terrain, 3-D surface objects with surface shadowing. The current capabilities of the code are unique, and are highlighted by use of a rigorous radiative transport approach and a full 3-D treatment of the atmosphere that includes finite clouds, surface BRDF effects, and a faceted surface description incorporating surface elevation and 3-D objects. The major drawback of the DSMC technique, however, is that it is too computationally intensive to support modeling of the 3000 km swaths of VIIRS-type sensors. The bulk of its computation time is spent calculating transmittances along photon paths.

Numerical weather prediction (NWP) models, such as the Pennsylvania State University (PSU) National Center for Atmospheric Research (NCAR) Fifth-Generation Mesoscale Model (MM5), have also been used to synthesize satellite data for algorithm development. Posselt et al. (2003) used MM5 fields to synthesize surface and atmospheric state variables for the Geosynchronous Imaging Fourier Transform Spectrometer (GIFTS) forward model and for retrieval algorithm development. In this system, MM5

produces high spatial- and temporal-resolution simulations used to produce a "truth" atmosphere, whose values were then passed through the GIFTS radiative transfer model to generate simulated TOA radiances. Temperature, water vapor, and winds retrieved from these radiances were subsequently compared with the original MM5 atmosphere to assess retrieval accuracy. The strength of this system is that surface data and atmospheric volume are self-consistent and that the radiative transfer calculations are computationally fast. This system, however, does not use separate atmospheric paths when calculating the different radiance contributions reaching the sensor.

Whereas previous image simulation systems have not included the horizontally inhomogeneous nature of the atmosphere in conjunction with a 3-D mesoscale meteorological model, the technique presented here accomplishes this by the integration of two widely used community models: MM5 and MODTRAN. These models were integrated with an electro-optical (EO) sensor-model describing the NPOESS VIIRS sensor and with an orbit model. A geophysical data cube (GDC), based on the MM5 system, was used as the basis for TOA radiance calculation and as *a-priori* truth. To capture the meteorological variability along the 3000 km sensor swath, scans were broken up into cells, with meteorological values interpolated to the locations of individual pixels. For each cell, the GDC was then probed along multiple slant paths to generate input profiles for MODTRAN. The paths describe the solar incident path onto the pixel, hemispheric downwelling radiance from the atmosphere, and radiance along the sensor path from the ground to the satellite. Selected phenomenological radiance components along the paths were then combined to generate the final radiance reaching the sensor aperture. Gener-

ated TOA radiance scenes were then used to construct the final sensor output products, known as Sensor Data Records (SDR), upon which various exploitation algorithms are designed to work. This system was developed during the Program Definition and Risk Reduction (PDRR) phase of the NPOESS proposal from the Lockheed Martin team.

2. Methodology

Transmittance and radiance along an atmospheric path is principally dependent on the amount and distribution of absorbing, emitting, and scattering species along the path (Berk et al. 2001). Figure 1 illustrates the simplest paths associated with the flux of photon energy onto a satellite sensor aperture. Some of the paths in fact represent the infinite-series sum of multiple scattering contributions. It is clear from the figure that photons reaching the sensor pass through different atmospheric profiles, and that the total radiance L_{sensor} reaching the sensor is the sum at the top of the atmosphere of each radiance value for each path (fluxes L_A-L_H):

$$L_{sensor} = L_A + L_D + L_B + L_E + L_G + L_H + L_C + L_F . \quad (1)$$

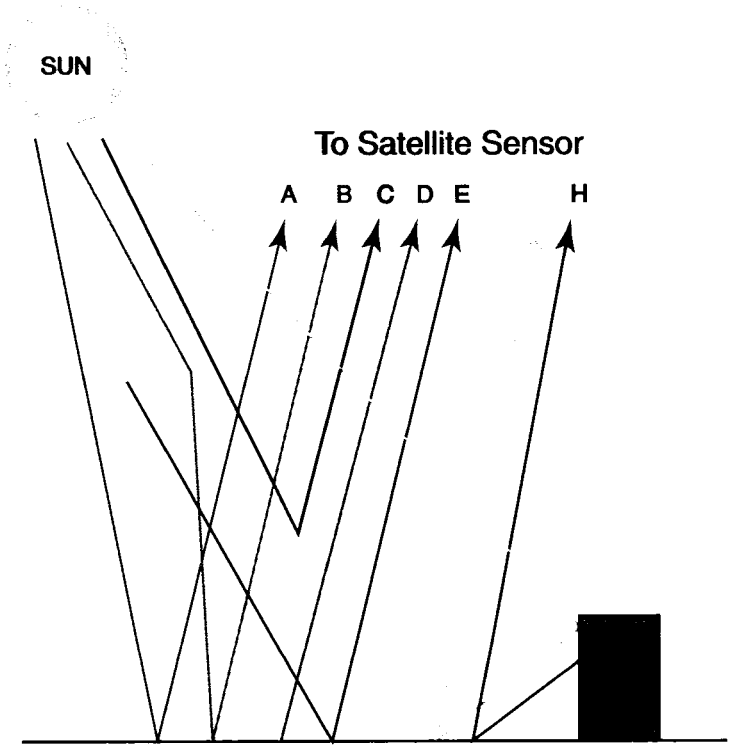

Fig. 1. Energy paths associated with the photon flux to a satellite sensor. Adapted from Schott (1997).

Substitution of mathematical expressions for the radiances in Eq. (1), assuming a Lambertian target, gives

$$
\begin{aligned}
L_{Sensor} = {} & E_{S\lambda}\cos(\sigma_{zenith})\tau_1\frac{r(\lambda)}{\pi}\tau_2 + \\
& \varepsilon(\lambda)L_{T\lambda}\tau_2 + \\
& F_{sky}E_{ds\lambda}\frac{r(\lambda)}{\pi}\tau_2 + \\
& F_{sky}E_{d\varepsilon\lambda}\frac{r(\lambda)}{\pi}\tau_2 + \\
& (1-F_{sky})L_{bs\lambda}r(\lambda)\tau_2 + \\
& (1-F_{sky})L_{b\varepsilon\lambda}r(\lambda)\tau_2 + \\
& L_{us\lambda} + \\
& L_{u\varepsilon\lambda}\,,
\end{aligned}
\tag{2}
$$

where all symbols are defined in Appendix A. A derivation of each term in is given in Schott (1997). The physical meanings of each term are:

(A) Pixel reflected radiance due to solar path incident spectral irradiance

(B) Pixel reflected spectral downwelling due to scattering (e.g., skyshine)

(C) Spectral upwelling radiance from the atmosphere due to scattering

(D) Spectral thermal radiance emitted by the pixel

(E) Pixel reflected spectral thermal radiance from downwelled emission

(F) Spectral thermal upwelling path radiance

(G) Spectral reflected radiance from the background scattering onto the target

(H) Spectral reflected radiance due to background emission onto the target.

The current multi-spectral image (MSI) simulation system (Fig. 2) has been developed to generate arrays of band-integrated EAR values for all pixels in each scan from an orbiting, multi-spectral whiskbroom scanning system, such as the NPOESS VIIRS sensor. The approach allows for multiple slant-path profiles of atmospheric quantities to be extracted from a database of meteorological and terrestrial parameters for a predetermined region of interest (i.e., a MM5 domain). This integrated system of models supports collection and scanning effects, including non-homogeneous atmospheric forward calculations, detector offset, scan overlap, and variable pixel sizes across a scan.

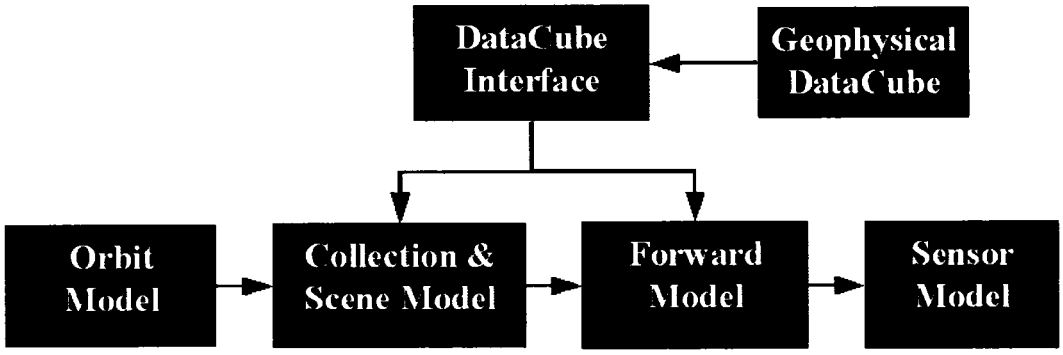

Fig. 2. High-level schematic of MSI modeling system.

a. MM5

The Fifth Generation Mesoscale Model (MM5) developed by Penn State University (PSU) and the National Center for Atmospheric Research (NCAR) is a sigma-coordinate model designed to simulate mesoscale atmospheric circulations. It is supported by several pre- and post-processing programs, which in addition to MM5 are re-

ferred to collectively as the "MM5 modeling system." The system is comprised of approximately 500 000 lines of Fortran code and is suitable for both single processor workstations, as well as for shared- and distributed-memory parallel computing environments. MM5 is one of the most widely used numerical weather prediction models and has been used to simulate atmospheric flows on horizontal scales with 1 to 120 km grid resolutions. A global version of MM5 (i.e., no lateral boundaries) has recently been formulated and tested (Dudhia and Bresch 2002).

1) FORMULATION

MM5 equations are fully compressible (non-Boussinesq) and non-hydrostatic; and its only approximation is neglecting the heating term in the pressure perturbation equation (Dudhia 1993). The model uses a terrain-influenced sigma coordinate system, ignores molecular diffusion, and uses Reynolds (decomposed and averaged) parameterized diffusion.

Variables are first decomposed into Reynolds averaged and turbulent components, e.g., for pressure

$$\hat{p} = p + p'', \tag{3}$$

where averaged variables are further decomposed into a reference state and flow induced perturbation:

$$p(x,y,z,t) = p_0(z) + p'(x,y,z,t). \tag{4}$$

The general set of governing dynamic and thermodynamic equations (before decomposition into their reference state and flow induced perturbations) in a rectangular

coordinate system (Holton 1992, Bluestein 1992, Pielke 2002) include the following five prognostic (u, v, w, ρ, q) and three diagnostic equations (ω, p, Q):

Momentum (x-component):

$$\frac{\partial u}{\partial t} = -\frac{1}{\rho}\frac{\partial p}{\partial x} - \vec{\mathbf{V}} \bullet \nabla u + 2\vec{\Omega} v \sin\phi - 2\vec{\Omega} w \cos\phi + F_x \tag{5}$$

Momentum (y-component):

$$\frac{\partial v}{\partial t} = -\frac{1}{\rho}\frac{\partial p}{\partial y} - \vec{\mathbf{V}} \bullet \nabla v - 2\vec{\Omega} u \sin\phi + F_y \tag{6}$$

Momentum (z-component):

$$\frac{\partial w}{\partial t} = -\frac{1}{\rho}\frac{\partial p}{\partial z} - g + 2\vec{\Omega} u \cos\phi + F_z \tag{7}$$

Compressible continuity:

$$\frac{\partial \rho}{\partial t} = -\nabla \bullet (\rho \vec{V}) \tag{8}$$

First law of thermodynamics:

$$dQ = c_v dT + p d\alpha = c_p dT - \alpha dp \tag{9}$$

Omega:

$$\frac{dp}{dt} = \omega = \frac{\partial p}{\partial t} + \vec{V}_H \bullet \nabla p - w\frac{\partial p}{\partial z} \tag{10}$$

Ideal gal law:

$$p = \rho R_d T \tag{11}$$

Moisture:

$$\frac{\partial q_n}{\partial t} = -\vec{\mathbf{V}} \bullet \nabla q_n - q_n \bullet \nabla \vec{\mathbf{V}} + S_n + D_n \quad , \tag{12}$$

where $n = 1,2,3$ for the solid, liquid, and vapor moisture phases, respectively, and where S_n represents moisture sources and sinks and D_n is diffusion.

The σ- (terrain influenced) coordinate transformation is defined by:

$$\sigma = \frac{p_0 - p_t}{p_s - p_t}, \tag{13}$$

where p_s and p_t are independent of time. Total pressure is thus

$$p = p^* \sigma + p_t + p', \tag{14}$$

where $p^*(x,y) = p_s(x,y) - p_t$ and where the 3-D dynamic pressure perturbation p' is a predicted quantity.

The general coordinate transformation from $(x,y,z) \rightarrow (x,y,\sigma)$ is:

$$\left(\frac{\partial}{\partial x}\right)_z \rightarrow \left(\frac{\partial}{\partial x}\right)_\sigma - \frac{\sigma}{p^*}\frac{\partial p^*}{\partial x}\frac{\partial}{\partial \sigma}. \tag{15}$$

Using the x-component of the pressure gradient force $\frac{1}{\rho}\frac{\partial p}{\partial x}$ as an example:

$$\left(\frac{1}{\rho}\frac{\partial p}{\partial x}\right)_z \rightarrow \left(\frac{\partial p}{\partial x}\right)_\sigma - \frac{\sigma}{p^*}\frac{\partial p^*}{\partial x}\frac{\partial p}{\partial \sigma}, \tag{16}$$

where $p(x,y,z,t) = p_0(z) + p'(x,y,z,t)$. As $\frac{\partial p_0(z)}{\partial x} = 0$,

$$\left(\frac{1}{\rho}\frac{\partial p'}{\partial x}\right)_z \rightarrow \frac{1}{\rho}\left[\left(\frac{\partial p'}{\partial x}\right)_\sigma - \frac{\sigma}{p^*}\frac{\partial p^*}{\partial x}\frac{\partial p'}{\partial \sigma}\right], \tag{17}$$

where the right hand side of (17) is the horizontal pressure gradient force in the sigma coordinate system.

Three map projections are available within MM5: Polar stereographic, Lambert conformal, and Mercator. Polar stereographic is preferred for high-latitude studies, Lambert conformal for middle-latitude studies, and Mercator for low-latitude studies. The Mercator projection was used for the current simulations and subsequent data processing, as it simplified the interpolation and indexing scheme that interfaced the sensor and radiative transfer models to MM5.

Although grid size ($\Delta x = \Delta y = \Delta s$) is constant, distances represented by Δs on the spherical earth varies with location. Map scale factor m is thus defined as:

$$m = \frac{\text{distance on model grid}}{\text{actual distance on earth}}. \tag{18}$$

For the Mercator projection, latitude $\phi(Y = 0)$ corresponds to the equator, and thus the relationships between X, Y, ϕ, and λ are

$$X = (r_{earth} \cos\phi_1)(\lambda - \lambda_0), \tag{19}$$

$$Y = (r_{earth} \cos\phi_1) \ln\left[\tan\left(45^\circ + \frac{\phi}{2}\right)\right] \tag{20}$$

$$Y = (r_{earth} \cos\phi_1) \ln\left[\frac{1+\sin\phi}{\cos\phi}\right], \tag{21}$$

where $(\lambda - \lambda_0)$ is in radians. The latitude ϕ_1 at which the Mercator projection is true is often taken as 30° N, as in the current study. X and Y are obtained from ϕ and λ by:

$$\lambda = \lambda_0 + \frac{X}{r_{earth} \cos\phi_1} \tag{22}$$

$$\phi = -90^\circ + 2\arctan\left[\exp\left(\frac{Y}{r_{earth}\cos\phi_1}\right)\right]. \tag{23}$$

2) TRANSFORMED EQUATIONS

In the following set of equations, the virtual temperature perturbation $T'_v = T_v - T_0$, replaces T, and thus $\rho = p/R_d T_v$. The value of c_p is modified for moist air, while $\gamma = c_p / c_v$ is assumed constant irrespective of water vapor content. The reference state is assumed dry, a liquid drag term $g(q_c+q_r)$ is added to the buoyancy term (Dudhia 1993), and the temperature diffusion term contains a correction for horizontal pressure differences. The equations presented below are from the MM5 V3 users guide (Dudhia et al. 1999) (henceforth MM5UG).

The 3-D pressure term is derived from the fully compressible mass-continuity equation and the ideal gas law by decomposition of Reynolds averaged pressure into static and mesoscale-flow induced parts as in (4), and by use of Eqs. (8)-(11) to yield:

$$\frac{dp'}{dt} = -\gamma p \nabla \bullet \vec{\mathbf{V}} + \frac{\gamma p}{T}\frac{\dot{Q}}{c_p}, \tag{24}$$

where $\dot{Q}$ is the diabatic heating term *(dQ)*. Expansion of the left hand side of (24) by use of (10) yields

$$\frac{\partial p'}{\partial t} + \mathbf{V} \bullet \nabla p' - \rho_0 g w = -\gamma p \nabla \bullet \vec{\mathbf{V}} + \frac{\gamma p}{T}\frac{\dot{Q}}{c_p}, \tag{25}$$

where $\rho_0 g = -\partial p / \partial z$ is the hydrostatic part. Rearrangement of terms yields the final form of the pressure tendency equation:

$$\frac{\partial p'}{\partial t} - \rho_0 g w + \gamma p \nabla \bullet \vec{\mathbf{V}} = -\mathbf{V} \bullet \nabla p' + \frac{\gamma p}{T}, \tag{26}$$

which neglects the diabatic pressure-perturbation term $(\dot{Q}/c_p + T_0 D_\theta / \theta_0)$. The term is considered negligible in most meteorological applications, since it only causes a small divergence (i.e., expansion) in regions of heating. Diabatic heating does enter this equation, however, through T via Eq. (31).

The following final momentum equations were derived from Eqs. (5)-(7), along with the map and sigma coordinate relationships developed previously.

Momentum (x-component):

$$\frac{\partial u}{\partial t} + \frac{m}{\rho}\left(\frac{\partial p'}{\partial x} - \frac{\sigma}{p*}\frac{\partial p*}{\partial x}\frac{\partial p'}{\partial \sigma}\right) = -\vec{\mathbf{V}} \bullet \nabla u + v\left(f + u\frac{\partial m}{\partial y} - v\frac{\partial m}{\partial x}\right) - ew\cos\alpha - \frac{uw}{r_{earth}} + D_u \tag{27}$$

Momentum (y-component):

$$\frac{\partial v}{\partial t} + \frac{m}{\rho}\left(\frac{\partial p'}{\partial y} - \frac{\sigma}{p*}\frac{\partial p*}{\partial y}\frac{\partial p'}{\partial \sigma}\right) = -\vec{\mathbf{V}} \bullet \nabla v + v\left(f + u\frac{\partial m}{\partial y} - v\frac{\partial m}{\partial x}\right) - ew\cos\alpha - \frac{vw}{r_{earth}} + D_v \tag{28}$$

Momentum (z-component):

$$\begin{aligned}\frac{\partial w}{\partial t} - \frac{\rho_0}{\rho}\frac{g}{p*}\frac{\partial p'}{\partial \sigma} + \frac{g}{\gamma}\frac{p'}{p} = -\vec{\mathbf{V}} \bullet \nabla w + g\frac{p_0}{p}\frac{T'}{T_0} - \frac{gR_d}{c_p}\frac{p'}{p} \\ + e\left(u\cos\alpha - v\sin\alpha\right) - \frac{u^2 + v^2}{r_{earth}} + D_w ,\end{aligned} \tag{29}$$

where *eu* and *ew* represent the usually neglected Coriolis components, $u\frac{\partial m}{\partial y}$ and $v\frac{\partial m}{\partial x}$ and r_{earth} curvature effects, and D_{xyz} parameterized molecular diffusion.

The temperature tendency equation is derived in a similar manner to the pressure tendency equation. Starting with Eqs. (9) and (11) and noting that $c_p = c_v - R$, it is straightforward to arrive at

$$c_p \frac{dT}{dt} = \frac{1}{\rho} \frac{dp}{dt} + \dot{Q}. \tag{30}$$

Expansion of the right hand side of (30), by use of Eq. (10) and rearrangement of terms yields the final temperature tendency equation:

$$\frac{\partial T}{\partial t} = -\vec{\mathbf{V}} \bullet \nabla T + \frac{1}{\rho c_p} \left(\frac{\partial p'}{\partial t} + \vec{\mathbf{V}} \bullet \nabla p' - \rho_0 g w \right) + \frac{\dot{Q}}{c_p} + \frac{T_0}{\theta_0} D_\theta. \tag{31}$$

The treatment of moisture in MM5 is divided into explicit and implicit schemes. Explicit schemes (e.g., cloud microphysics) treat resolved precipitation physics, while implicit schemes (e.g., cumulus parameterization) treat non-resolved precipitation physics; both may simultaneously operate at a given grid-point. Additional options allow for either dry runs, where moisture is treated as a passive variable (explicit and implicit schemes not applied), or "fake dry runs," where latent heat effects are removed (Grell et al. 1995).

Resolvable scale precipitation processes are activated whenever grid-scale saturation is reached. The simplest approach, still sometimes used in larger scale models, simply removes super-saturation as precipitation and adds the latent heat to the thermodynamic equation. More sophisticated schemes carry additional variables, such as cloud, rainwater, ice, and snow, dependent on the selected cloud microphysics, cumulus parameterization, and shallow convection options.

For completeness, it is necessary to expand the advection and divergence terms to show the effects of the coordinate transformation. Expansion of the advection of general variable A yields:

$$\vec{\mathbf{V}} \bullet \nabla A \equiv mu\frac{\partial A}{\partial x} + mv\frac{\partial A}{\partial y} + \dot{\sigma}\frac{\partial A}{\partial \sigma}, \tag{32}$$

where

$$\dot{\sigma} = \frac{d\sigma}{dt} = \frac{\rho_0 g}{p^*}w - \frac{\sigma}{p^*}\left(u\frac{\partial p^*}{\partial x} + v\frac{\partial p^*}{\partial y}\right). \tag{33}$$

Divergence is expanded as

$$\nabla \bullet \vec{\mathbf{V}} = m^2\frac{\partial}{\partial x}\left(\frac{u}{m}\right) - \frac{m\sigma}{p^*}\frac{\partial p^*}{\partial x}\frac{\partial u}{\partial \sigma} + m^2\frac{\partial}{\partial y}\left(\frac{v}{m}\right) - \frac{m\sigma}{p^*}\frac{\partial p^*}{\partial y}\frac{\partial v}{\partial \sigma} - \frac{\rho_0 g}{p^*}\frac{\partial w}{\partial \sigma}, \tag{34}$$

where p^* is constant over flat surfaces.

3) PARAMETERIZATIONS

MM5 contains boundary layer, surface layer, radiation, cumulus, and microphysical options that vary significantly in complexity and computational recourse requirements. For example, precipitation and microphysics options range from a dry model to simple removal of super-saturation to mixed phases with graupel, snow, and hail. Boundary layer diffusion/mixing formulations range from simple bulk to high resolution K-profiles to well-mixed layers with cloud effects on radiation. MM5 includes prognostic equations for water vapor and microphysical variables (such as clouds and precipitation) that include source and sink terms. The following discuss the diffusion, sub-grid mixing, and physics options chosen for this study.

MM5 has the following two types of generalized horizontal diffusion (second and fourth order) to control nonlinear instability and aliasing:

$$F_{H2\alpha} = p^* K_H \nabla_\sigma^2 \alpha \tag{35}$$

and

$$F_{H4\alpha} = p^* K'_H \nabla_\sigma^4 \alpha\,, \tag{36}$$

where $K'_H = \Delta s^2 K_H$. Second-order diffusion is only used in the coarsest domain for grid-point rows and columns adjacent to lateral boundaries, while fourth order is used for the remainder of the coarse domain and for all sub-domains.

The horizontal diffusion coefficient K_H consists of a background value K_{H0} and a term proportional to deformation D

$$K_H = K_{H0} + 0.5k^2 \Delta s^2 D\,, \tag{37}$$

where D is given by Smagorinski *et al.* (1965) as

$$D = \left[\left(\frac{\partial u}{\partial x} - \frac{\partial v}{\partial y} \right)^2 + \left(\frac{\partial v}{\partial x} + \frac{\partial u}{\partial y} \right)^2 \right]^{1/2} \tag{38}$$

and where K_H is a function of grid size and time step via:

$$K_{H0} = 3 \times 10^{-3} \frac{\Delta x^2}{\Delta t}\,. \tag{39}$$

The horizontal operators ∇^4 and ∇^2 are applied on constant sigma surfaces, and to ensure computational stability, an upper limit of $\frac{\Delta x^2}{64\Delta t}$ in imposed on K_H. Errors associated with use of horizontal operators on sigma surfaces near steep terrain (where sigma surfaces are nearly vertical) may require a new sigma formulation.

The Reynolds-averaged tensor-form of the Navier-Stokes equations, neglecting molecular viscosity and Coriolis, is

$$\frac{\partial u_i}{\partial t} = -u_i \frac{\partial u_i}{\partial x_i} - \frac{1}{\rho}\frac{\partial p_i}{\partial x_i} + \delta_{i3} g - \frac{\partial \overline{(u_i' v_i')}}{\partial x_i}, \tag{40}$$

where the last term (represented by T_i) is turbulence flux-divergence due to unresolved (sub-grid-scale) motions. Expansion of its u-component yields

$$T_x = -\frac{\partial \overline{(u'u')}}{\partial x} - \frac{\partial \overline{(u'v')}}{\partial y} - \frac{\partial \overline{(u'w')}}{\partial z}, \tag{41}$$

which can be parameterized by use of K-theory as

$$T_x = -\frac{\partial}{\partial x}\left(K_x \frac{\partial u}{\partial x}\right) - \frac{\partial}{\partial y}\left(K_y \frac{\partial u}{\partial y}\right) - \frac{\partial}{\partial z}\left(K_z \frac{\partial u}{\partial z}\right). \tag{42}$$

Dependent on the physics options chosen in MM5, the first two terms in Eq. (42) are ignored in mesoscale applications (to save CPU time), as horizontal grid spacing is typically an order of magnitude larger than vertical grid spacing and as horizontal gradients are usually smaller than vertical gradients. The final term is thus almost always several orders of magnitude larger than the first two. This assumption, however, does not hold at cloud scales, where the first two can be larger than the third (Bryan and Fritsch 2003).

The National Canter for Environmental Prediction (NCEP) Oregon State University Air Force office of Hydrology land surface model (NOAH/LSM) was used in the current application to predict soil-moisture and temperature at four layers (10, 30, 60, and 100 cm). It also predicts canopy moisture, water-equivalent snow depth, and surface and underground run-off accumulations. It uses vegetation and soil types for evapotranspira-

tion and includes soil conductivity and gravitational moisture flux. It also interacts with the MM5 medium range forecast (MRF) planetary boundary layer (PBL) scheme by taking its surface boundary layer (SBL) exchange coefficients, radiative forcing, and precipitation rate as input, and outputs surface fluxes for the MM5 PBL scheme (Dudhia et al. 1999).

The surface skin temperature scheme of Mahrt and Ek (1984) uses a single linearized surface-energy balance equation that represents a vegetation surface cover (Chen and Dudhia 2000). The equation for soil temperature T is:

$$C(\Theta)\frac{\partial T}{\partial t} = \frac{\partial}{\partial z}\left[K_t(\Theta)\frac{\partial T}{\partial z}\right], \tag{43}$$

where volumetric heat capacity C and thermal conductivity K_t are functions of fractional volumetric soil water content Θ (Pan and Mahrt 1997).

The finite-difference form of equation (43) for the ith soil layer is:

$$\Delta z_i C_i \frac{\partial T_i}{\partial t} = \left(K_t \frac{\partial T}{\partial z}\right)_{z_{i+1}} - \left(K_t \frac{\partial T}{\partial z}\right)_{z_i}, \tag{44}$$

where the Crank-Nicholson scheme is used. To close the thermal diffusion term, the lower boundary (assumed as 3 m) temperature is needed. Because such observations are not generally available, annually averaged air temperatures from the European Centre for Medium-Range Weather Forecasts (ECMWF) are used. These data, however, depend on ECMWF orography and are sequentially adjusted to 1000 mb by use of the (low resolution) ECMWF and (high resolution) MM5 origraphies, analyzed surface pressures, and the standard atmosphere lapse rate (Chen and Dudhia 2000).

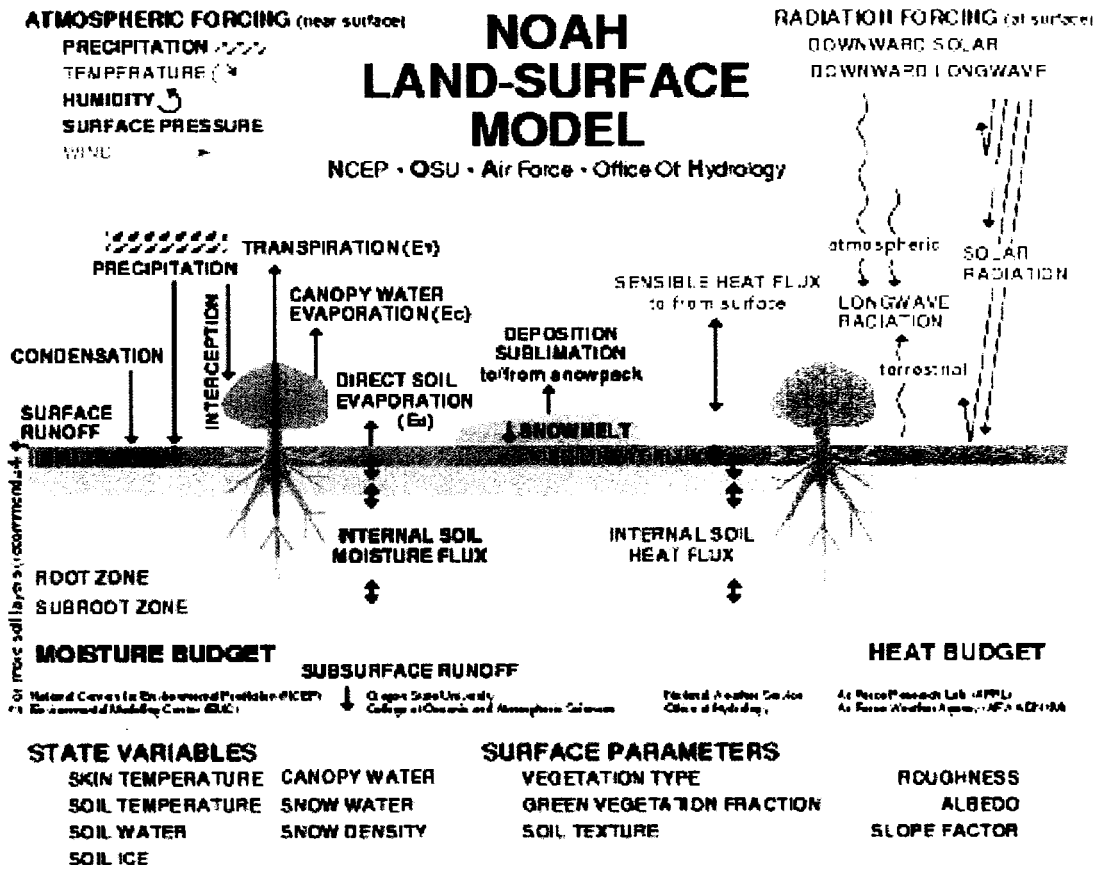

Fig. 3. Surface layer processes in the NOAH LSM and interactions with the atmospheric boundary layer. Adapted from Chen and Dudhia (2001).

The NOAH/LSM also handles sea-ice, snow cover, and frozen soil effects. In addition to soil moisture, soil water is a separate four-layer variable and soil moisture is the total of soil water and soil ice (Chen and Dudhia 2001).

The MRF PBL scheme must be used with the NOAH/LSM scheme. It is a first order closure that parameterizes the diffusion of heat, moisture, and momentum in the lowest kilometer of the atmosphere. It determines the vertical extent and intensity of mixing based upon the stability of the lowest model layer (Fig. 4).

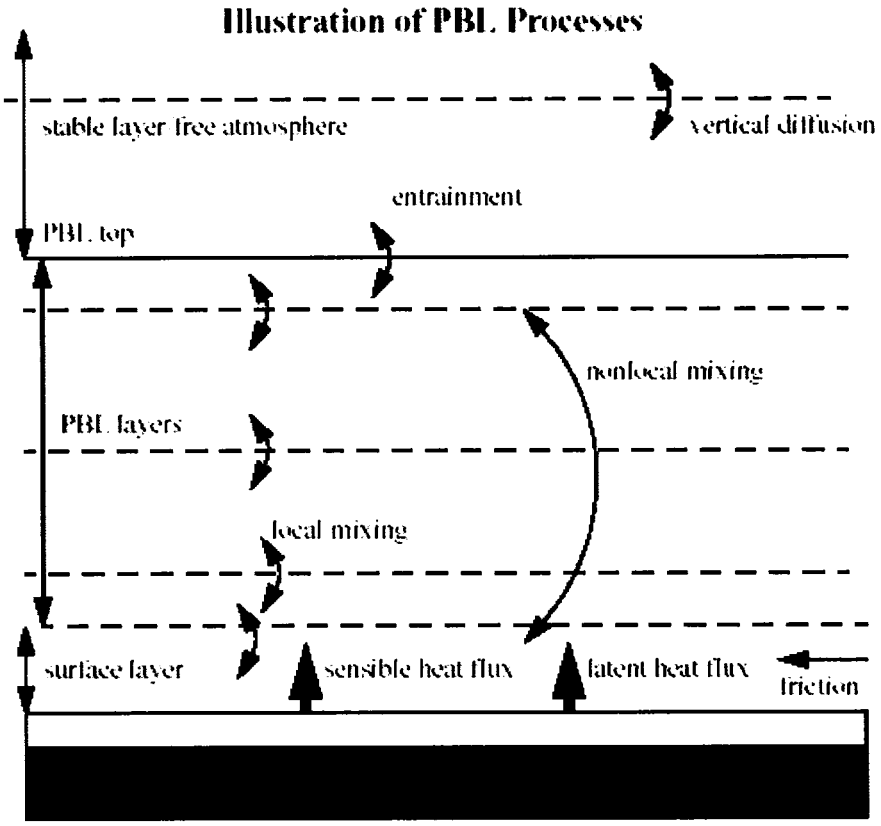

Fig. 4. PBL processes in MM5. Adapted from Dudhia et al. (1999).

The MRF PBL scheme is a computationally efficient *K*-profile method that uses a counter-gradient correction in well-mixed PBLs to construct temperature, moisture, and wind profiles. Turbulent kinetic energy is not calculated and no direct interactions exist with microphysics or radiative processes in the free atmosphere, although computed cloud fields can cross the interface between the free atmosphere and boundary layer. When the surface layer is stable, the intensity of mixing is determined by the magnitude of the Richardson number. When the layer is unstable, the vertical extent and intensity of mixing are determined by the convective boundary layer lapse rate and by the sensible

heat flux near the ground. Heat, moisture, and momentum can also cross between the boundary layer and free atmosphere, as they can in the real atmosphere. Because the MRF-PBL somewhat simplifies vertical profiles, some fine-scale structures may not be well resolved.

Non-dimensional SBL wind shear and buoyancy parameters ϕ_M and ϕ_θ are derived using Dyer and Hicks. For unstable regimes, $\overline{(w'\theta')} \geq 0, L \leq 0$, the relationships for U and for θ and q, respectively, are:

$$\phi_M = \left(1 - 16\frac{0.1h}{L}\right)^{-1/4}, \tag{45}$$

$$\phi_\theta = \left(1 - 16\frac{0.1h}{L}\right)^{-1/2}. \tag{46}$$

For stable regimes, $\overline{(w'\theta')} < 0, L > 0$, they become:

$$\phi_M = \phi_\theta = \left(1 - 5\frac{0.1h}{L}\right), \tag{47}$$

where L is the Monin Obukhov (MO) length:

$$L \equiv \frac{u_*^2 \overline{\theta}}{kg\theta_*}, \tag{48}$$

and h is the height of the lowest model layer.

Mixed layer PBL diffusion is based on large eddy simulations (Troen and Mahrt 1986), in which turbulent diffusivity coefficients are calculated from a prescribed profile as a function of boundary layer height and scale parameters that consider counter gradient

turbulent mixing. Free atmosphere diffusion is based on scale parameters obtained from observations (Kim and Mahrt 1992, Kennedy and Shapiro 1980).

The prognostic equation for general PBL variable A by use of K theory is:

$$\frac{\partial A}{\partial t} = \frac{\partial}{\partial z}\left[K_A \left(\frac{\partial A}{\partial z} - \gamma_A \right) \right], \tag{49}$$

where $\gamma_A = b\frac{\overline{(w'A')}}{w_s h}$ is the counter gradient term and $w_s = u_* \phi_M^{-1}$ is the mixed layer velocity scale. (Hong 1999) In the mixed layer:

$$K = k w_s z \left(1 - \frac{z}{h} \right)^{p_K}, \tag{50}$$

where p_K is not specified in the documentation. Use of $\phi_M = \phi_\theta = 1$ for calm conditions can produce unrealistic values of K, which is related to ϕ_M and ϕ_θ through the mixed layer velocity scale w_s. According to (Shir and Bornstein 1976), any use of $\phi_M = \phi_\theta = 1$ in K-theory should be re-evaluated.

The Dudhia (1989) radiation scheme includes long- and short-wave interactions with clouds (water drops and ice) and clear air (water vapor and carbon dioxide). The scheme (Fig. 5) also accounts for surface radiation fluxes and it produces atmospheric temperature tendencies from radiative processes. Shortwave absorption depends upon water vapor and carbon dioxide distributions in clear or cloudy air. These effects are also included for longwave absorption and emission; however, the shortwave and longwave calculations do not interact explicitly. For this experiment, radiative fluxes were only updated every 30 minutes.

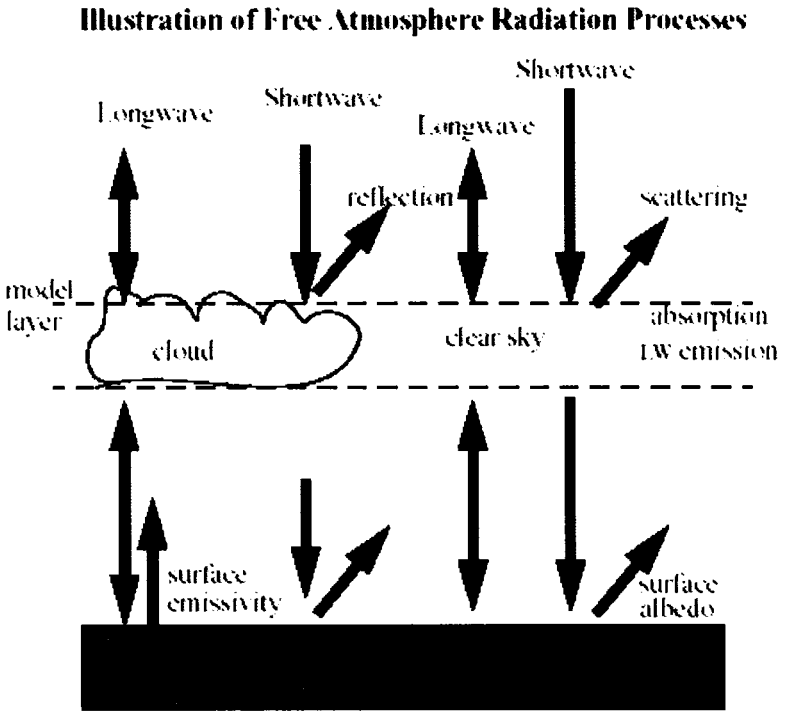

Fig. 5. Radiation processes in MM5. Adapted from Dudhia et al. (1999).

The shortwave flux depends on solar zenith angle, cloud albedo, absorption effects on shortwave radiation, clear air scattering, and water-vapor absorption. The scheme considers longwave absorption and emission by water vapor and carbon dioxide. Surface short- and long-wave fluxes are used in the surface energy balance calculation.

Limitations include that only stratiform clouds are considered and that, for a given grid box, cloud fraction is either 0 or 100%. AFWA forecasters have also noted that MM5 generally underestimates nocturnal surface cooling, which has implications for surface temperature forecasts and affects PBL cooling.

The Reisner et al. (1988) mixed-phase explicit moisture scheme predicts cloud liquid water, cloud ice, rainwater, snow mixing ratios, and ice fields, and it allows for super-

cooled water and for ice at temperatures slightly above freezing. While it has no graupel or riming processes, it does feed the liquid and ice fields back into the convective scheme (Fig. 6). The resolvable precipitation physics removes super-saturation as precipitation. In addition, the precipitation and cloud parameterization scheme allows ice phase processes at temperatures less than 0° C, when cloud water is treated as cloud ice particles and rain is treated as snow.

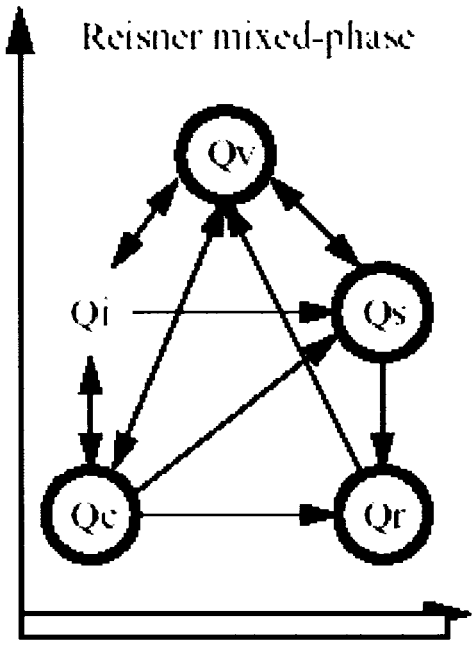

Fig. 6. Reisner mixed-phase cloud microphysics scheme in MM5. Adapted from Dudhia et al. (1999).

The equations for water vapor, cloud water and ice, and rain water and snow, respectively, are:

$$\frac{\partial p^* q_v}{\partial t} = -m^2\left[\frac{\partial p^* u q_v / m}{\partial x} + \frac{\partial p^* v q_v / m}{\partial y}\right] - \frac{\partial p^* u \dot{\sigma}}{\partial \sigma} - \vec{\mathbf{V}} \bullet \nabla q_v + p^*(-P_{RE} - P_{CON} - P_{II} - P_{ID}) + D_{qv} \tag{51}$$

$$\frac{\partial p^* q_c}{\partial t} = -m^2\left[\frac{\partial p^* u q_c / m}{\partial x} + \frac{\partial p^* v q_c / m}{\partial y}\right] - \frac{\partial p^* u \dot{\sigma}}{\partial \sigma} - \vec{\mathbf{V}} \bullet \nabla q_c + p^*(-P_{ID} - P_{II} - P_{RC} - P_{PA} - P_{CON}) + D_{qv} \tag{52}$$

$$\frac{\partial p^* q_r}{\partial t} = -m^2\left[\frac{\partial p^* u q_r / m}{\partial x} + \frac{\partial p^* v q_r / m}{\partial y}\right] - \frac{\partial p^* u \dot{\sigma}}{\partial \sigma} - \vec{\mathbf{V}} \bullet \nabla q_r - \frac{\partial V_f \rho g q_r}{\partial \sigma} + p^*(-P_{RE} - P_{CON} - P_{II} - P_{ID}) + D_{qv} \quad . \tag{53}$$

All relevant processes assume a Marshall-Palmer size distribution, and droplet fall speeds are taken as $V(D) = aD^b$. For rain, the Marshall-Palmer intercept parameter is $N_0 = 8\text{x}10^6\ m^{-4}$, a = 841.99667, and $b = 0.8$, while for snow $N_0 = 2\text{x}10^7\ \text{m}^{-4}$, $a = 11.72$, and $b = 0.41$. Its advantages include that it accounts for super-cooled water and that grid-scale precipitation effects on other meteorological variables are explicitly calculated, which produces accurate precipitation distributions, as fewer thermodynamic assumptions are made.

The Grell et al. (1991) cumulus parameterization scheme (Fig. 7) assumes deep convective clouds of only one size. It also ignores direct lateral entrainment or detrainment, except at the origin or termination of updrafts and downdrafts, which implies a constant with height mass flux. Since lateral mixing is ignored, it is not necessary to assume a small fractional area-coverage of updrafts and downdrafts, which allows the scheme to operate easily at finer scales (Pielke 2002). The scheme is thus well adapted for horizontal grids as fine as 10 to 12 km. Figure 8 summarizes the direct interactions of the above-discussed physical parameterizations.

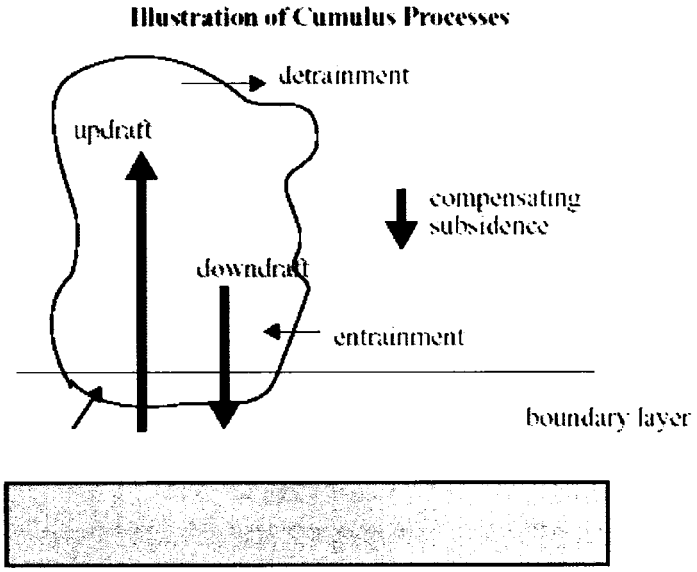

Fig. 7. Modeled cumulus processes in MM5. Adapted from Dudhia et al. (1999).

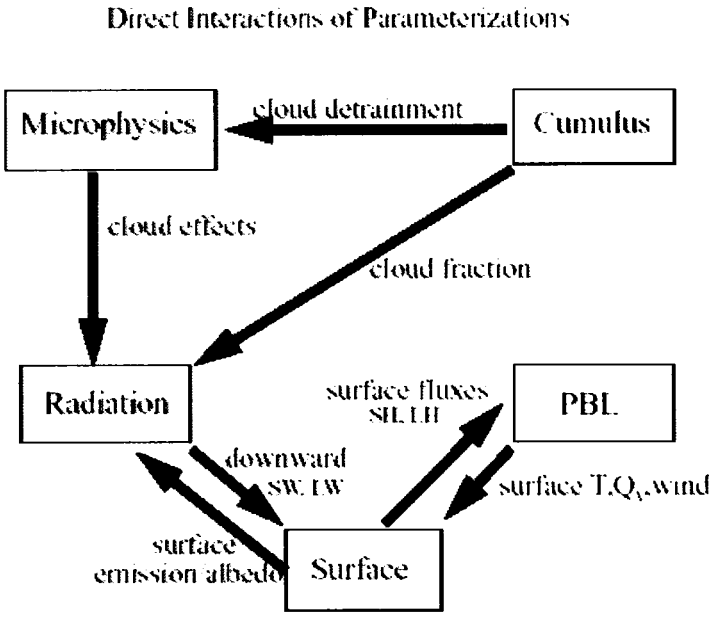

Fig. 8. Modeled cumulus processes in MM5. Adapted from Dudhia et al. (1999).

4.) NUMERICS

MM5 uses an Arakawa-Lamb B-staggering grid with scalar products (such as temperature, mixing ratio, and pressure) defined at grid square centers and with u and v velocity components defined at grid square corners (Fig. 9).

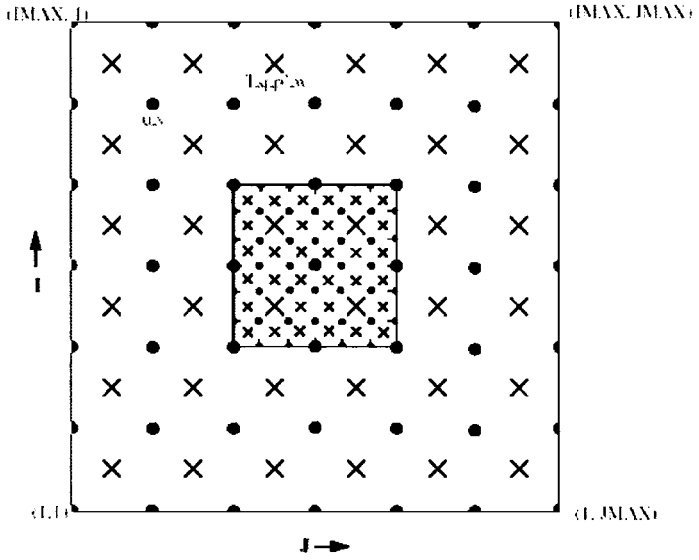

Fig. 9. Arakawa-Lamb B-staggering grid configuration showing scalar (dot) and velocity (cross) points. Inner box is a 3:1 coarse to fine-grid inner mesh. Adapted from Dudhia et al. (1999).

Staggered grids effectively increase horizontal resolution by a factor of two (as information comes from adjacent grid points) and can reduce solution separation problems associated with leapfrog time differencing on non-staggered grids (Haltiner and Williams 1980). Arakawa and Lamb (1977) examined various 2-D grids and concluded that the B grid is best when the Rossby radius of deformation $L_R = (g/h)^{1/2}/f$ is smaller that the grid size. While B grids require half the time step of un-staggered grids, they

give better structure for the shorter waves that can arise from geostrophic adjustment after initialization, small scale heating nonlinear interactions, or mountains (Haltiner and Williams 1980).

The MM5 vertical grid is composed of full and half sigma levels, with vertical velocity calculated at grid box centers and with scalars and horizontal velocities defined at half levels (Fig. 10).

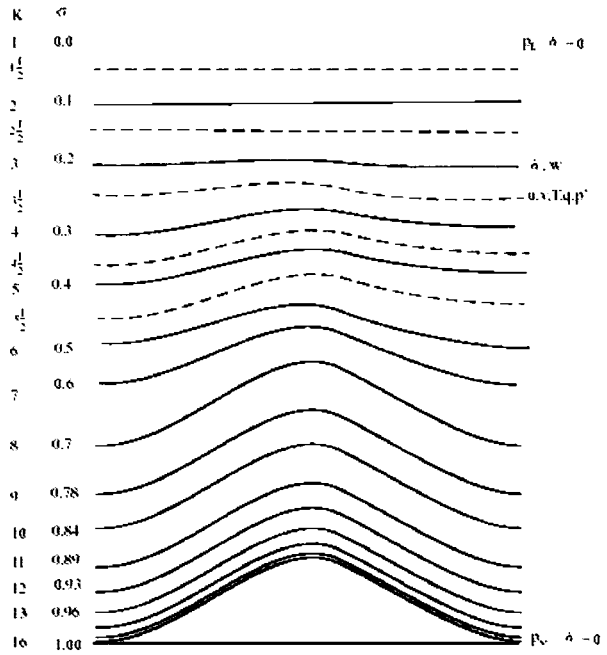

Fig. 10. MM5 terrain-influenced sigma vertical grid, where dashed lines represent half sigma levels and solid lines full sigma levels. Adapted from Dudhia et al. (1999).

In Eqs. (26)-(29) and (31), second-order centered finite differences are used to represent gradients, except for the precipitation fall term, which uses a first-order upstream scheme for positive definiteness. Horizontal averaging is often required to determine gradients at correct grid positions and vertical interpolation allows for a variable vertical grid size (Dudhia et al. 2003).

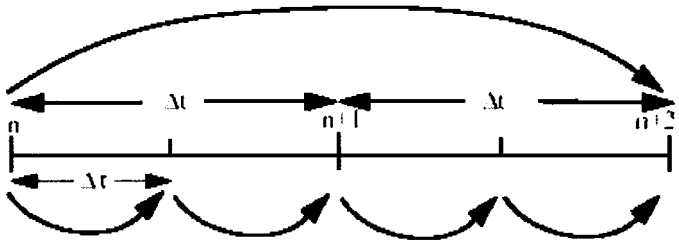

Fig. 11. MM5 time splitting long- and short-leapfrog time steps scheme. Adapted from Dudhia et al. (1999).

A second-order leapfrog time-step scheme is used; however, some terms are handled using a time splitting (Fig. 11). Note that Eqs. (26)-(29) contain extra terms on their left hand sides that are responsible for sound waves and must be calculated on even shorter time steps. In leapfrog schemes, tendencies at time *n* are used to step variables from time n-1 to n+1. This is used for most of the right-hand terms (i.e., advection, Coriolis, buoyancy). Forward steps are used for diffusion and microphysics, where tendencies are first calculated at time n-1 and then used to step variables from n-1 to n+1.

Some radiation and cumulus options use a constant tendency over many model time steps and are only recalculated every 30 minutes. For certain terms, the model time step is too long for stability and these have to be predicted with shorter steps, e.g., the precipitation fall term and PBL tendencies (which also may be split). When time steps are split, certain variables and tendencies are updated more frequently. Sound wave u, v, w, and p' need to be updated by four short step by use of the tendency terms on the left of Eqs: (26)-(29), during which the right hand terms are kept fixed (Dudhia et al. 2003).

Certain processes in MM5 are treated implicitly for numerical stability. Implicit time schemes have tendencies that depend not only on present and past values, but also on fu-

ture values. These schemes are often numerically stable for all time steps, but usually require a matrix inversion to implement them. MM5 implicit schemes are used only in 1-D column calculations for vertical sound waves and vertical diffusion, so that the matrix is tri-diagonal, making it straightforward to invert (Dudhia et al. 2000).

5.) INITIAL AND BOUNDARY CONDITIONS

MM5 initial conditions are derived by interpolation of data from a larger scale model, such as the AVN, to the MM5 grid. Time interpolation may also be necessary when no large-scale model analysis is available and for boundary conditions during the simulation period. Support programs REGRID and INTERPF perform initial and boundary condition generation. REGRID reads the large-scale model grids and interpolates data to the horizontal MM5 grid and then INTERPF vertical interpolates to sigma surfaces.

For coarse-domain lateral boundary conditions, MM5 uses relaxation-inflow/ outflow boundary conditions, which allow larger-scale migratory features to propagate into the mesoscale domain and migratory mesoscale features to flow out, thereby avoiding reflection and noise. The outer row and column of the coarse grid are specified and the next four are nudged towards analysis fields. This allows the higher resolution MM5 physics to determine the solution; however, the region of interest should be far from the lateral boundaries (or within a nested region) to avoid direct influences from the large-scale model. Inner-domain boundary values and tendencies come from the parent domain and are updated at each time step, with the outer two rows and columns specified as

a no-relaxation zone, which allows outer-domain solutions to directly influence inner-domain solutions.

Upper and surface boundary and initial conditions are also necessary. Equation (33) reduces to 0 at the upper and lower boundaries, $\sigma = 0$ and $\sigma = 1$, respectively. A zero-gradient or "free-slip" condition is employed to obtain horizontal velocities at these boundaries (Dudhia 1992). MM5 employs a radiative upper boundary condition with the full 3-D Coriolis force to allow gravity waves to radiate through the model without reflection. The surface model interacts with the MRF PBL scheme by taking surface-layer exchange coefficients, radiative forcing, and precipitation rate as inputs, and by outputting surface fluxes for the PBL scheme. The bottom boundary condition of the surface model (at 3 m) is the annually averaged air temperature from the ECMWF.

b. MODTRAN

In the early 1970s, the Air Force Cambridge Research Laboratory initiated a program to develop computer-based atmospheric radiative transfer algorithms. The first attempts translated the graphical procedures of McClatchey et al. (1970, 1972), based on empirical transmission functions and effective absorption coefficients derived primarily from controlled laboratory measurements. That spectrally averaged atmospheric transmittance does not obey the Beer-Lambert Law at any but the finest spectral resolution was already well known. The resulting Low Resolution Transmittance (LOWTRAN) code was first released in 1972 (Selby et al. 1972). This effort has now progressed to a set of codes and related algorithms (including line-of-sight spherical geometry, direct and

scattered radiance and irradiance, and non-local thermodynamic equilibrium) with improved accuracy, efficiency, and accessibility (Anderson et al. 1995).

MODTRAN4 (Berk et al. 1996) is the U.S. Air Force (USAF) standard moderate spectral-resolution radiative-transport model for wavelengths extending from the thermal infrared (IR), through the visible and into the ultraviolet (0.2 to 10 000 μm). The MODTRAN4 radiative transport model, developed by Spectral Sciences, Inc. and the USAF Research Laboratory, is based on a 1 cm^{-1} statistical band model coupled to a correlated-*k* (CK) algorithm. It provides a fast alternative (100-fold increase in speed) to the USAF first principles and more accurate line-by-line (LBL) radiative transport models: FASCODE4 and FASCODE for the Environment, and FASE5. Comparisons between MODTRAN4 and FASE spectral transmittances and radiances show agreement to within a few percent or better in the thermal IR (Berk et al. 2001) and even smaller errors when integrating over wider bands

MODTRAN4 includes flux and atmosphere-scattered solar calculations (essential for analysis of near-IR and visible spectral region data), not readily generated by LBL models. One limitation of MODTRAN is that it assumes a horizontally stratified atmosphere and a spherical earth. Molecular, aerosol, and cloud densities are thus solely functions of altitude, and the ground is modeled as a uniform, constant altitude surface. For many real world problems, the horizontal *in*homogeneity of the atmosphere and ground greatly influences radiance signatures. In particular, shadowing (from clouds, vegetation, and surface structures), spatial variability of gaseous H_2O, and surface topography will complicate contrast signatures and increase scene clutter. MODTRAN4 and its predeces-

sors have been integrated into many imaging simulation models, which generally use MODTRAN to predict path spectral transmittances and radiances as a function of range for a fixed sensor-geometry. Transmittances are then multiplied by at-source signatures and added to path radiances to obtain apparent source signatures.

c. GDC

The Geophysical Data Cube (GDC) is designed to provide a multi-dimensional, multi-resolution database of weather observations (e.g., RAOB, SAO, and satellite), gridded data from numerical weather modes (e.g., MM5 and AVN), static data (e.g., topography and land use), and derived variables (e.g., derived cloud mask from MM5 output). Information from this database is extracted by query functions to generate atmospheric state vectors and surface data to support TOA radiance calculations (Fig. 12).

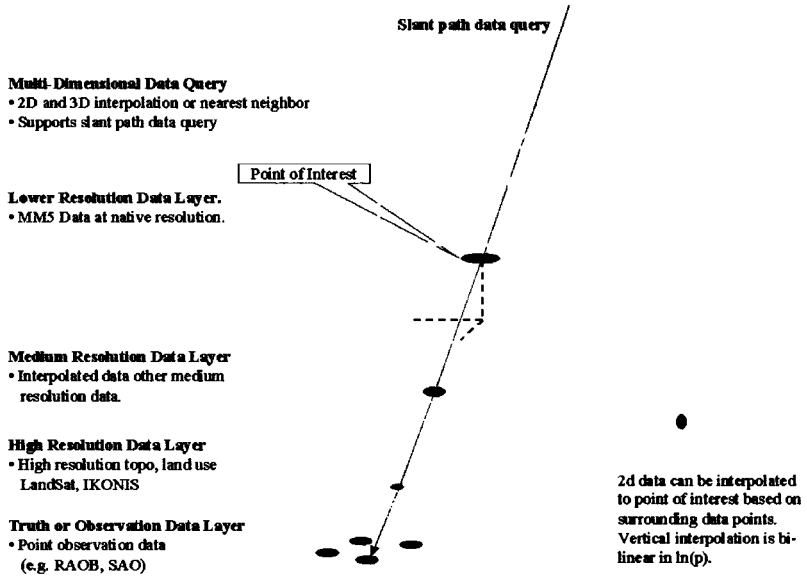

Fig. 12. Conceptual illustration of the Geophysical Data Cube (GDC) and the relationship between multi-dimensional and multi-resolution data.

The relationship between multi-dimensional and multi-resolution data within the GDC is an important feature of the HSI modeling system. Consider an example where multiple atmospheric state profiles and surface data are extracted from the GDC for points on the earth separated by about 1 km. For each query, temperature and moisture profiles may change little, since they are driven by the relatively low resolution MM5 data. The high-resolution surface data associated with each query, however, may return a different surface material type, temperature, and digital elevation map (DEM) value, since they are driven by the high-resolution global data sets. While many GDC data sets are global, MM5 domains are regional. Since the current simulations were based primarily on MM5 data, the global database has regions of particular interest; this study focused on a West Coast domain.

A GDC is generated before the simulation for the time and region of interest. It includes fixed information about surface type and altitude, as well as temporal meteorological information about both surface and overlying atmospheric volume. The latter information is synthesized from a variety of sources, including space borne sensors, surface instrumentation, and numerical weather data. The GDC is defined by the MM5 domain and includes (but is not limited to) pressure, temperature, humidity, wind, and ozone density, along with ice, snow, and cloud-layer coverage maps.

All variables within the GDC can be accessed via a set of query functions. These query functions are part of a standard I/O interface, known as an Application Programmers Interface (API) that generally links code and/or data sets. This API interfaces the

TOA radiance software (based on MODTRAN) and the GDC. The GDC API developed for the current application is a Fortran 90 library that can be linked to (and called by) C, C++, and/or Fortran codes.

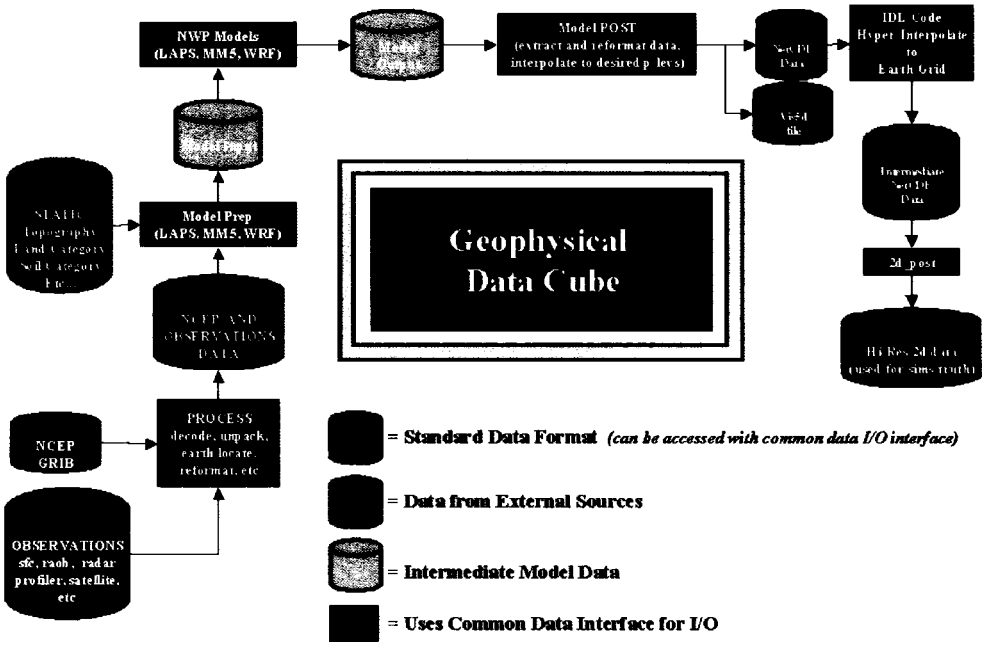

Fig. 13. Flow of data used to generate the GDC, where blue data containers are all part of the GDC and in the NetCDF standard data format.

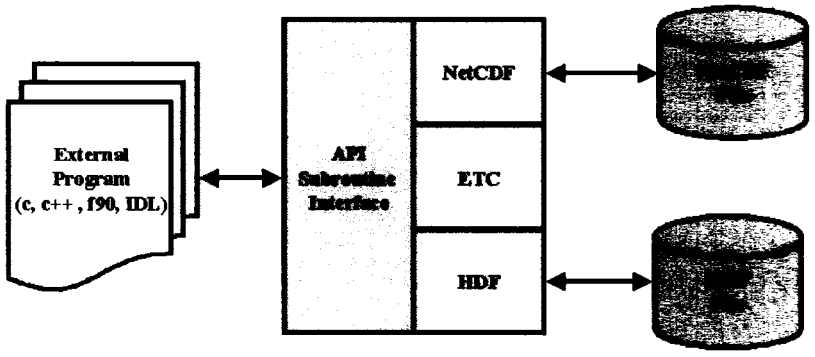

Fig. 14. High-level schematic of the GDC API.

The GDC API interface library consists of two layers: (a) low-level interface (set of compact NetCDF routines) designed to handle redundant file and variable bookkeeping and (b) high-level routines designed to serve major functions. For example, the GDC query routine "get_surface_temp" returns surface temperature for a location in time and space. Before the value is returned to the calling routine, however, the following internal data processing is performed: (a) establishing and opening correct file for domain of interest and then b) loading latitude, longitude and temperature data into arrays. The I/O of "get_surface_temp" is performed by the low-level interface, which are transparent to the calling routine.

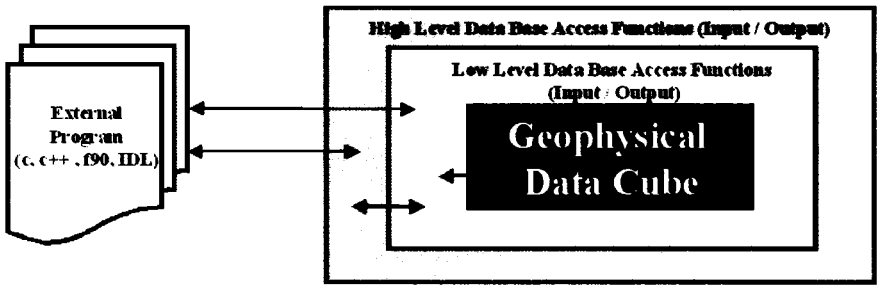

Fig. 15. Relationship between the GDC and both API layers.

The six main query routines used between the GDC, sensor model, and MODTRAN are:

- get_surface_alt – This routine extracts surface topography altitude from the GDC at the given latitude and longitude. Since topography is a large global dataset, sections of data are tiled in and out of memory to maximize processing speed and minimize memory usage.

- get_surface_mat – This routine extracts surface material from the GDC. A mathematical relationship is used to map latitude and longitude input values to array index values based on the Goode Homolosine projection.
- get_2d_atmosphere – This routine returns 2 m air temperature, moisture, and wind components, based on MM5 data, from the GDC. The MM5 data are interpolated on the fly in this routine by use of a weighted bi-linear technique.
- get_3-D_atmosphere – This routine extracts 3-D atmospheric quantities, based on MM5 output, from the GDC. One value each of temperature, moisture, pressure, cloud liquid water and ice, and ozone are returned for each latitude, longitude, altitude, and time value. Repeated queries are necessary to extract a complete profile. Values are interpolated on the fly by use of horizontal bi-linear and vertical logarithmithic bi-linear techniques.
- get_cloud_info – This routine returns cloud mask and cloud fraction information for both ice and water clouds for each latitude and longitude value. 2-D cloud data, derived from MM5 fields, are interpolated to a pre-defined grid before this step.
- get_surface_temp – This routine returns surface temperature for a given latitude, longitude, and time value. The 2-D surface temperature, derived from MM5, is interpolated to a pre-defined grid before this step.

With all the above routines, I/O from disk is performed only on the first call to the query routine by the low-level functions. After the initial call, a query routine takes approximately 1.0×10^{-6} seconds per call. For the VIIRS radiometric EDR grid, the retrieval

of surface temperature takes approximately 8.5 s for $9.0x10^6$ subroutine calls, a speed possible because no searching is involved to extract a temperature value for a given latitude-longitude pair. One feature of the GDC and the API is the geometrical relationship developed between a latitude-longitude pair and array indices. For high-resolution interpolated products, a pre-defined grid was established and values interpolated to given points.In conjunction with the 1 km resolution, 24-category land-use and topography values, several other 2-D data sets are generated by use of MM5 output: surface temperature, snow cover, water cloud mask and fraction, and ice cloud mask and fraction. Surface temperature and snow cover are generated from MM5 NOAH/LSM variables, while cloud variables are generated from MM5 3-D cloud variables.

For the spectral region that can penetrate the atmosphere and "see" the surface, it is important to have all surface data co-registered to the identical latitude longitude grid. During early simulations, it became apparent that the relatively lower (20 km) resolution MM5 surface temperature data were causing radiometric errors near coastal regions, where land surface temperature (LST) values were being used as sea surface temperature (SST) values and vice-versa. To correct this, an algorithm was developed to interpolate the MM5 data to 1 km resolution using information from higher resolution land use and topography data. The algorithm, which uses a combination of IDL and Fortran 90 code, can be explained at a top level as follows:

i) Generate a 1 km resolution latitude-longitude grid of land use and topography

ii) Interpolate MM5-LSM surface temperatures to 1 km grid

iii) Use land-use data to identify coastal regions and generate land-sea mask

iv) "Erode" surface temperature data away from coastal regions

v) Interpolate surface temperature data back to "eroded" areas based on land use data from surrounding points at similar elevations.

The core of the algorithm contains small corrections for altitude using MM5 2 m air temperature and topography values, as well as smoothing of sea surface temperatures to remove numerically generated gradients (Fig. 17).

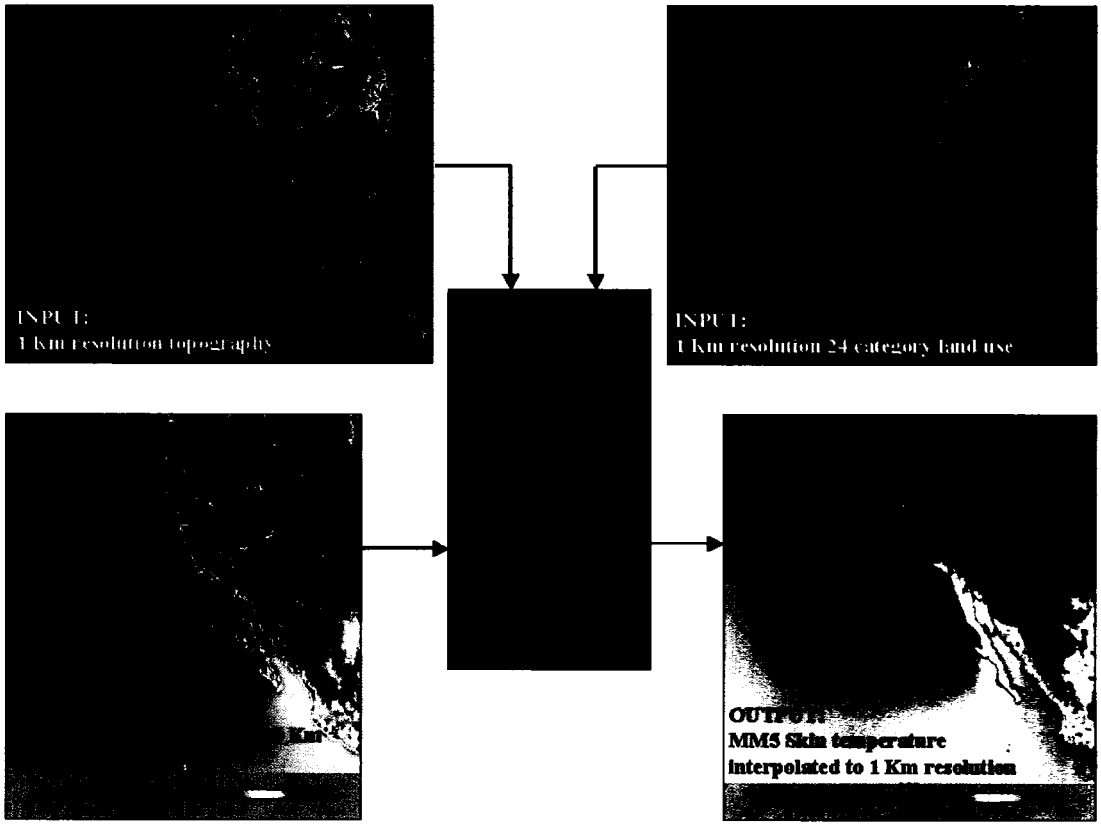

Fig. 16. High-level data flow for interpolating MM5-LSM surface temperature to 1 km horizontal resolution by use of 1 km resolution topography and land use information. Boxes around San Francisco Bay and Santa Barbara areas represent comparison regions in Fig. 17.

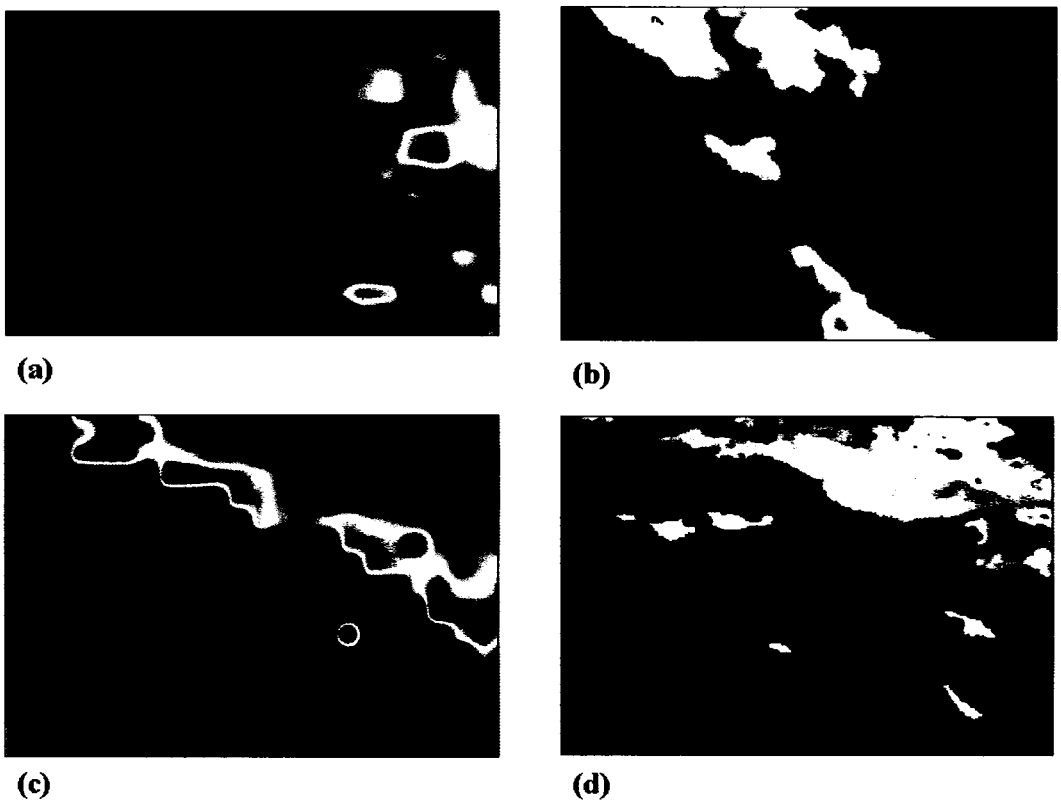

Fig. 17. San Francisco Bay Area and Santa Barbara skin temperatures, where (a) and (c) are MM5 20 km resolution outputs and (b) and (d) are interpolated 1 km values. Images are histogram stretched to highlight features.

The cloud query routine returns four cloud variables on the identical grid as surface temperature: liquid water cloud mask, ice cloud mask, liquid water cloud fraction, and ice cloud fraction. To interpolate MM5 cloud data, cloud liquid water and cloud ice mixing ratios were vertically integrated on the native MM5 grid. These 2-D files were then interpolated to approximately 1 km horizontal resolution. For mask products, integrated cloud ice or cloud water values > 1.0×10^{-5} g kg^{-1} were considered a cloud, while for cloud fraction products, integrated values were scaled to values between zero and one.

Fig. 18. MM5 cloud fields at 1900 UTC on 22 October 2000, where: (a) is total cloud mask, (b) integrated cloud liquid water, and (c) integrated cloud ice.

d. MM5 configuration

For this study, MM5 was configured to run on a Sun Ultra 80 UNIX workstation running Solaris 8 with two 750MHz Sun-Sparc processors and 2 GB Ram. The code was compiled with GNU Make version 3.78 with the Sun HPC version 6.1 Fortran 90 compiler.

Physics options and domains were chosen to satisfy the needs of subsequent data processing. The domain size was chosen large enough (Fig. 19) to simulate five minutes of the NPOESS polar orbiting satellite flying the VIIRS and CMIS sensors. To summarize the configuration: (NX, NY, NZ) = (220, 260, 24), $\Delta x = \Delta y = 20\,\text{km}$, time step = 60 s, integration time = 900 s, start time = 22 October 2000 at 0600 UTC, central latitude and longitude = (32.0 N, 122.0 W), Reisner mixed phase cloud physics, Grell convective parameterization, MRF PBL scheme, Dudhia radiation, NOAH/LSM, and initial and boundary conditions from the NCEP-AVN 1 degree global model.

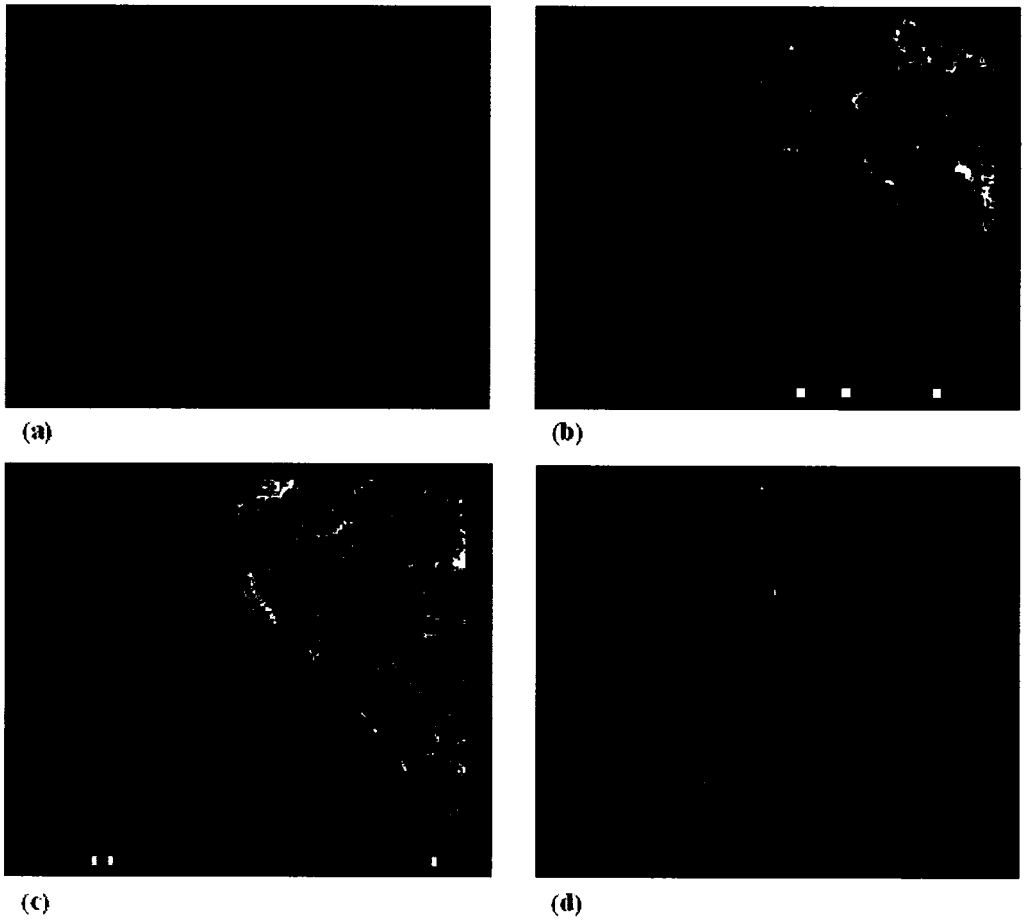

Fig. 19. Mercator grid MM5 inputs: (a) domain outline, (b) soil type, (c) land use, and (d) terrain height.

e. TOA radiance modeling

The software developed for the TOA radiance calculations for this study has evolved over several years. The original Radiometric Environmental Correction Algorithm applied to MODtran (RECAMOD) system of Cipperly and Wilcox (1999) was developed at the Integrated Systems and Solutions division of Lockheed Martin Space Systems Company. The range of capabilities encompassed by the MODTRAN based RECAMOD system was extended prior to the NPOESS proposal era to become a princi-

pal component of what is now called the Advanced Remote Sensing System (ARSS). The ARSS was then further developed to perform multi-spectral simulations in support of Lockheed Martin demonstrations to the government in pursuit of the NPOESS contract. The basic developmental approach began with the original ARSS software, and during the NPOESS proposal era, was enhanced to generate TOA radiance data sets with sufficient fidelity to test and evaluate selected EDR algorithms for the VIIRS sensor (Cipperly 2002).

The TOA simulation consists of the execution of the following software modules for each scan: (1) simulation setup, (2) scenemaker, (3) metsetup, (4) RECAMOD, (5) EARmaker, (6) sensor modeling, and (7) output formatting. Steps (1)–(5) are described in this section, while the descriptions of steps (6) and (7) are beyond the scope of the current thesis. These steps are generally executed sequentially in the simulation of a given scan, but simulations for separate scans can be performed in parallel. UNIX scripts were used to execute the simulation modules for multiple scans, with the distribution among multiple processors done manually by setting up and launching separate scripts for each processor (Cipperly 2002).

To begin a simulation, the sensor orbital-track through the simulation region is calculated, which includes computing the start times for each scan along the sensor track. The program to calculate these sensor position and velocity parameters is not described in this document, but the end result is the creation of a set of directories (one per scan for a whisk broom scanning sensor).

Fig. 20. Relationship between sensor, orbit, 3-D earth, and GDC models.

Each directory is preloaded with a file that contains the initial time and the sensor position and velocity for the scan-readout period. A file pointing to all other necessary simulation parameter files is also placed in each directory. This allows the simulation for a given scan to be performed by a separate executable running in the directory for that scan, where it does not interfere with simultaneous program executions for other scans. This in turn allows the overall simulation to be expedited by running simultaneous scans on multiple processors and machines.

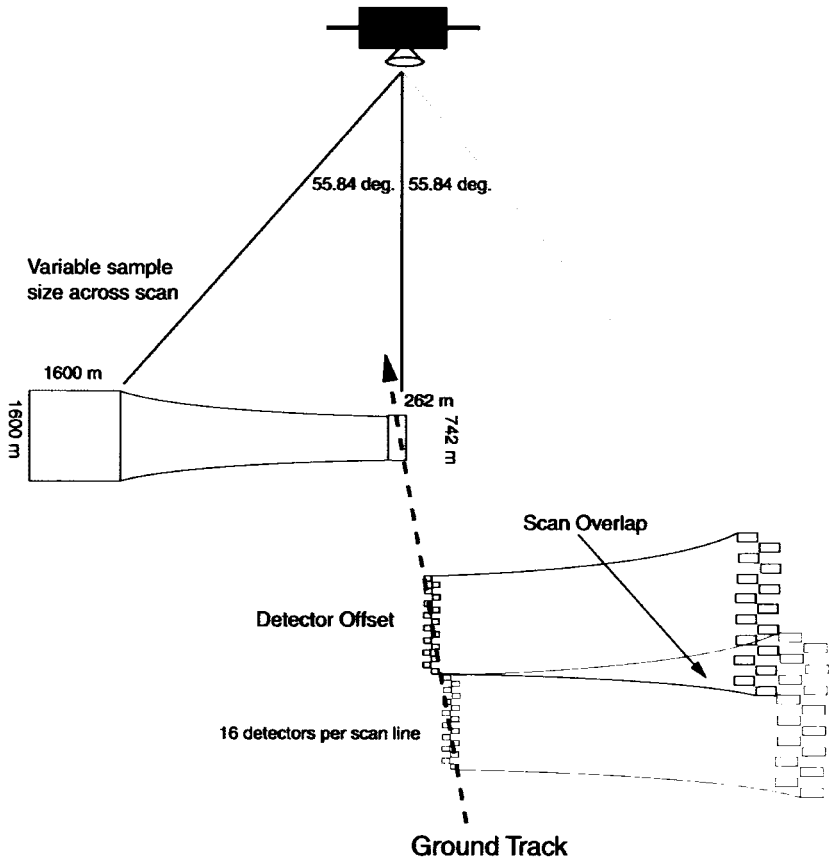

Fig. 21. VIIRS sensor model and pixel alignment on earth-surface. Adapted from Cipperly and Wilcox (1999)

For a whiskbroom scanner like VIIRS, the scenemaker program generates a scan by rotation of the scanning mirror or telescope around its specified rotation axis, and at the midpoint of every dwell time, propagating the center of each detector element through the optical system down to its intersection with the earth surface. It is actually the optical axis that is scanned, and pixel Instantaneous Field of View (IFOV) center lines-of-sight are defined by the angular offsets of detector element centers from the optical axis. The earth surface is defined by a topographic database of altitudes relative to the WGS84 Geoid (that defines Mean Sea Level).

Surface altitude is extracted from the GDC for a given latitude and longitude. By use of repeated topographic GDC queries, the line-of-sight from each detector center is iteratively propagated until it intersects with the Earth surface. Maximum of-nadir scan angle and the spatial resolution of the sensor are such that the incorporation of refractive bending of the lines-of-sight was not required. At this point, geodetic latitude, longitude, and altitude are recorded for the pixel IFOV center on the ground. Use of a topographic map causes the grid of IFOV centers to deviate from a grid of uniformly spaced points, particularly at the edges of scan regions with steep terrain gradients. Use of an iterative extension of the lines-of-sight allows for a line-of-sight to be intercepted by tall mountains before it would otherwise intersect the ground. This allows scenarios in which there is masking of terrain by closer features to be modeled, again particularly near the edge of scans (Cipperly 2002).

Solar zenith and azimuth angle and sensor zenith and azimuth angles are calculated for each pixel based upon the: (1) position of the center of the pixel IFOV on the ground, (2) position of sun, and (3) position of the sensor as propagated along its velocity vector from its position at the beginning of the scan to a position at the time the scan reaches the given pixel. These calculations involve a transformation to Earth Center Fixed (ECF) coordinates, where angle calculations are more straightforward (Cipperly 2002).

As with surface altitude, both surface temperature and relative humidity are extracted directly from the GDC for a given latitude and longitude for every pixel in the scene. In the case of surface (in reality 2 m) winds, the u and v components are extracted

and are converted to speed and azimuth within ARSS. Surface material types recognized by ARSS as configured for the NPOESS VIIRS demonstrations, and whose optical properties are included in its optical properties database, are currently the 17 surface types in the NASA/IGBP set. The GDC, however, incorporates the USGS 24 category surface-material types. A translation table included in ARSS allows the USGS surface material index obtained from GDC for each pixel to be transformed into the index of the most similar NASA/IGBP surface type, prior to saving the array of surface types (Table 1).

24 Category USGS	17 Category IGBP
0	0
1	13
2	12
3	12
4	12
5	12
6	12
7	10
8	6
9	7
10	9
11	4
12	3
13	2
14	1
15	5
16	17
17	11
18	11
19	16
20	16
21	16
22	16
23	16
24	15
99	16

Table 1. Transformation table to convert USGS 24 to IGBP 17 category surface material type.

The 17-category set actually includes three additional types: tundra (#18), fresh snow (#19), and sea ice (#20). Tundra is included as a special case of desert/barren (#16) in some NASA/IGBP documentations, as this as an 18th type. Fresh snow and sea ice, which appear in some other NASA/IGBP surface type descriptions, provide optical properties of the surface when a land or sea surface is indicated in the GDC as snow- or ice-covered.

Once scene arrays have been populated with all quantities at every pixel center, array files are created that contain latitude, longitude, altitude, solar zenith and azimuth angles and sensor zenith and azimuth angles, as well as surface material, temperature, relative humidity, wind speed, and wind azimuth values for each ground IFOV center. Along the way, various diagnostic quantities are also calculated, e.g., azimuth of a scan centerline projection onto the ground at the point nearest nadir (Cipperly 2002).

The scenemaker module is written largely in C, but must be compiled with a C++ compiler as it uses some C++ features. GDC querying functions are written in Fortran 90, and C and Fortran 90 object codes are linked using Fortran, which requires all functions to be written as C functions with names that Fortran can recognize.

The "metsetup" phase has two basic functions. The first constructs 2-D pixel coverage arrays for sea ice (only over water), snow (over land or ice), and multiple cloud layers. Two cloud layers were used in the current simulations, i.e., for ice and liquid water clouds, but the program is designed to process any number of layers. When parameters for multiple cloud layers are ingested, "metsetup" orders the layers from top to bottom, according to their cloud top height value. Time constraints preclude making

MODTRAN runs for every pixel, so each scan is divided into Meteorological Cells (Met Cells) with boundaries satisfying user specified size constraints, for which average meteorological properties are determined and separate MODTRAN runs made (Cipperly 2002).

This importance of the Met Cell concept cannot be overemphasized, as to run MODTRAN on every pixel in the scene, and often multiple times for each pixel, would take approximately one year for a VIIRS sensor simulation on a single processor workstation. The Met Cell concept (details proprietary) reduces the runtime to approximately two weeks, while maintaining spectral and spatial fidelity. For a wide scan, Met Cells near scan edges will contain many fewer samples than cells near nadir, due to elongation of ground IFOVs as a result of increasing sensor zenith angle due both to looking off to the side and Earth curvature.

The second principal function of metsetup is to lay out the Met Cells and determine surface properties for each: average surface temperature, most common surface material, and average relative humidity. After defining lines-of-sight vectors from the center of the Met Cell on the ground to both the sun (if present) and sensor, it extends these vectors from several points within each cell, queries the data cube to find atmospheric properties along each, and then averages profiles in each direction to get mean directional profiles along the vertical, sensor line-of-sight, and incident solar paths (Fig. 22). Any redundant (because they are nearly coincident) vectors are combined into a single profile to reduce the number of MODTRAN runs. For each retained profile in each Met Cell, a MODTRAN tape5 input file is automatically created, inserting the profile as a "user de-

fined profile" using the mean surface properties for the cell and the geometry pertinent to the cell-center (Cipperly 2002). These multiple profiles are the basis of the non-homogeneous nature of the radiative transport calculations.

In addition to the clear sky profiles, metsetup determines which cloud layers are present within each cell. For each such layer, a meteorological profile is retrieved from the data cube at its thickest point within the cell, and an additional MODTRAN tape5 file is created that includes cloud profile data for that layer. For the simulations presented here, two layers were retrieved: liquid water and ice. No mechanism is currently in place to distinguish cloud layer type, so all clouds are modeled as strato-cumulous of either all liquid water or ice. MODTRAN's cirrus model was not used, even though many of the ice clouds are in fact cirrus, because cirrus model input parameters are not directly available from the GDC. Among the diagnostic values generated by "metsetup" is the fractional coverage for each cloud layer, as well as for ice and snow, within the boundaries of each Met Cell.

To include the appropriate spectral range in the MODTRAN calculations, "metsetup" puts the sensor spectral bands in order, combines any which overlap, and determines an appropriate spectral sampling resolution for each (Cipperly 2002). In addition to creating the tape5 files themselves, "metsetup" automatically generates UNIX scripts to perform the required MODTRAN runs.

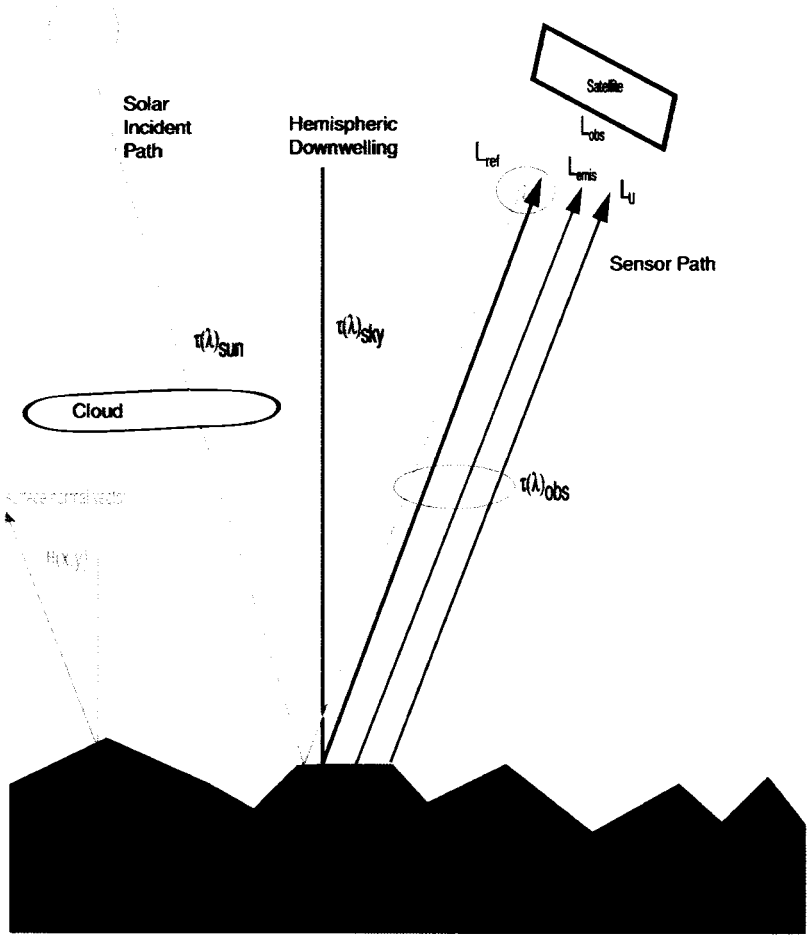

Fig. 22. Relationship between radiance paths and profiles extracted from the GDC. $\tau(\lambda)_{sun}$, $\tau(\lambda)_{sky}$, $\tau(\lambda)_{obs}$ are the atmospheric transmission functions for the solar incident, hemispheric downwelling and line of sight paths respectively. L_{ref}, L_u, L_{emis} are the radiance contributions from the reflected (solar incident and downwelling), upwelling and surface emissive respectively, and L_{obs} is the total at sensor radiance. T_{sfc} is skin temperature, ρ is surface reflectance and $\theta(x,y)$ represents the solar zenith angle. Reflective terms include thermal components.

One or more MODTRAN runs are made for each Met Cell, up to three clear air profile runs for the vertical, line-of-sight, and solar incident directions, and for the simulation discussed here, up to two cloud layer runs. While solar-sensor geometry is the same for each file in a cell, meteorological profiles are sampled along different paths

through the GDC, which can produce noticeably different results when looking at shallow angles toward regions with a great deal of horizontal variability in weather conditions (Cipperly 2002).

The ARSS is a significant evolution and extension of RECAMOD, which consists of pre-processing (building tape5 files), executing MODTRAN, and post-processing. The latter consist of combining directional MODTRAN results, converting to photons s^{-1}, performing sensor spectral band integration, and combining results calculated for separate directional profiles into a single file that can be read by the Entrance Aperture Radiance Maker (EARmaker).

The final processing step, EARmaker is software that ingests, combines, and processes outputs from the previous modules. Its technical details are proprietary, but in short, the following radiance components are added together to produce the total EAR data: path radiance (thermal, single scattered solar, and multiple scattered solar), ground reflected diffuse down-welling radiance (atmospheric thermal and solar skylight) scaled by the Directional Hemispheric Reflectance (DHR)), reflected direct solar scaled by the applicable bi-directional solar reflectance, and surface thermal emission scaled by one minus DHR. The spectral radiance for a pixel is then integrated over each spectral band of the sensor to produce mean (over time) band integrated radiance values, which are saved to files that contain arrays of band integrated EAR values for each pixel for subsequent processing in the VIIRS modeling process (Cipperly 2002).

The VIIRS sensor modeling is another extensive set of calculations, the details of which will not be discussed here. In short, this step adds realistic optical system effects

to the data reaching the ground. It includes, but is not limited to, application of a modulation transfer function (MTF), noise, calibration errors, stray light errors, detector offset, and spectral mixing.

3. Results

The simulation time was chosen to coincide with the over-flight of the Earth observing system (EOS) Terra satellite on 22 October 2000 at 1922 UTC. The goal is a direct comparison between simulated VIIRS data calibrated to SDRs and the observed moderate resolution imaging spectrometer (MODIS) level 1B SDR data, with the understanding that differences exist between the two instruments (e.g., band centers, band widths, optics, etc.). Level 1B, geolocation, and EDR data were acquired for this time in hierarchical data format (HDF) format from the EOS data information system (EOS-DIS).

Evaluation of the performance of the radiative transport modeling followed verification of the MM5 simulation. For quality TOA simulation data, the atmosphere must be accurately characterized, including its cloud placement and type, temperature and moisture profiles, and surface variables.

a. MM5 results

The overall synoptic pattern on 22 October was characterized by a closed circulation at 500 mb centered over North West Baja California, while a 300 mb jet streak propagated around a positively tilted trough axis that extended from western Utah to the Pacific Ocean west of Cabo San Lucas in Baja. This high amplitude trough pattern is associated with a cloud field (discussed later) over the South-Western U.S., with a weakening cold front extending southwest from central Baja. A surface low-pressure system was centered near southwestern Arizona with associated northerly flow over much of California.

To evaluate the MM5 produced synoptic pattern, Eta analysis fields that included upper air observations were acquired from NCEP for 22 October at 1200 UTC. These were only used in qualitative comparisons, since numerical data files were not available. For five significant levels (300, 500, 700, 850, and 925 mb), MM5 12-h forecasts were compared to NCEP fields to evaluate the position and timing of synoptic features.

The MM5 300 mb 12-h forecast for 22 October at 1200 UTC (Fig. 23) shows good agreement with the Eta model output. The Vandenberg (VBG) observation at this level is in particular good agreement with the MM5 temperature and wind velocity. The concurrent 500 mb (Fig. 24) MM5 12-h forecast for also shows good agreement with the analysis circulation center, as both show a closed center of circulation over NW Baja (see 5480 m geopotential height contour).

At 700 mb (Fig. 25), the MM5 12-h forecast again shows a closed center of circulation over NW Baja, the simulated 3000 m height counter, however, does not extend as far south as in the Eta analysis and the simulation shows a smaller 2970 m contour at this level. At 850 and 925 mb (Figs. 26 and 27), MM5 12-h heights and winds agree well with the analysis position of the center of circulation, but the MM5 height gradient is somewhat too strong. The simulated temperature values also agree well with the Eta analysis at these levels.

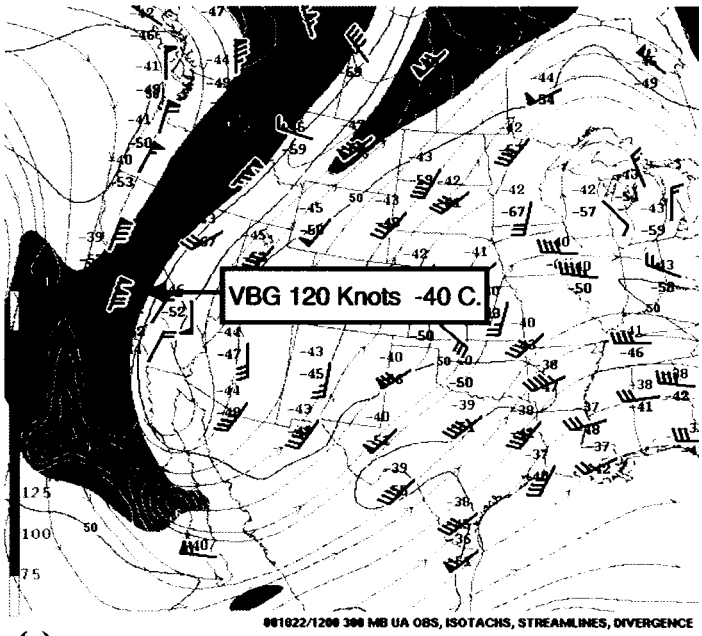

(a)

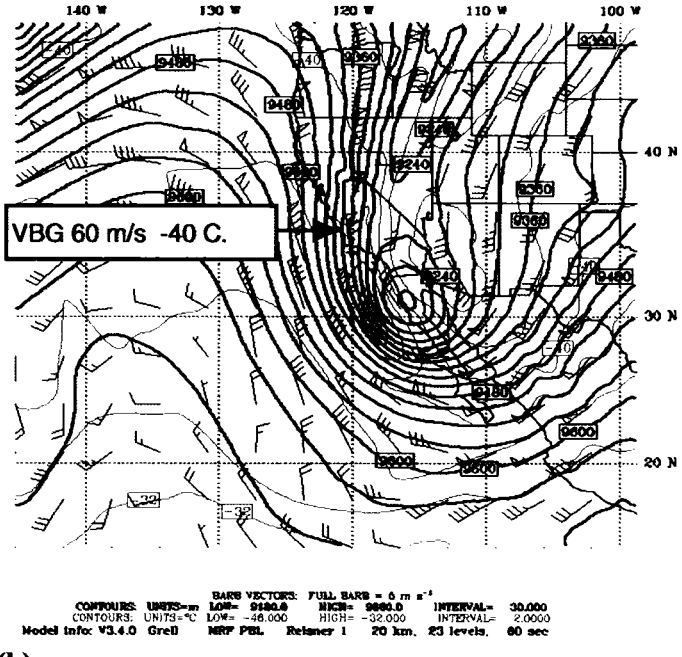

(b)

Fig. 23. Synoptic pattern for 300 mb at 1200 UTC on 22 October for (a) Eta, with streamlines (gray), isotachs (blue), divergence (yellow), and continental boundaries (dark gray). Observations show wind (blue, full barb = 10 kt), temperature (red, °C), and dewpoint (green, °C) and (b) MM5 12-h forecast, with heights (black, interval of 30 m), winds (blue, full barb = 5 m s^{-1}), and temperature (red, interval of 2°C).

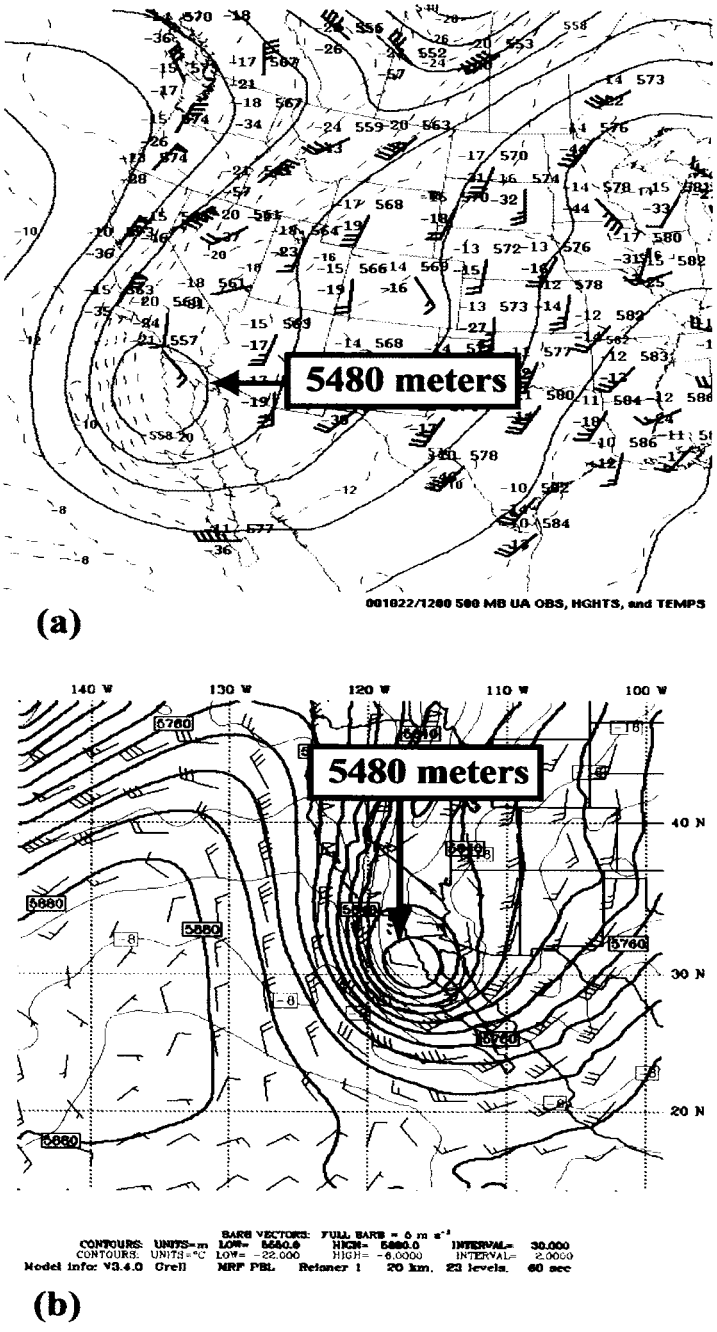

Fig. 24. Synoptic pattern at 1200 UTC on 22 October 2000 for (a) Eta 500 mb analysis with heights (gray, interval of 6 dm), temperature (interval of 1° C, red ≥ 0, blue < 0), and continental boundary's (dark gray). Observations show wind (blue, full barb = 10 kt), temperature (red, °C), and dewpoint (green, °C). MM5 500 mb 12 h forecast (b), with heights (black, interval of 30 m), winds (blue, full barb = 5 m s^{-1}), temperature (red, interval of 2°C), and continental boundaries (dark gray).

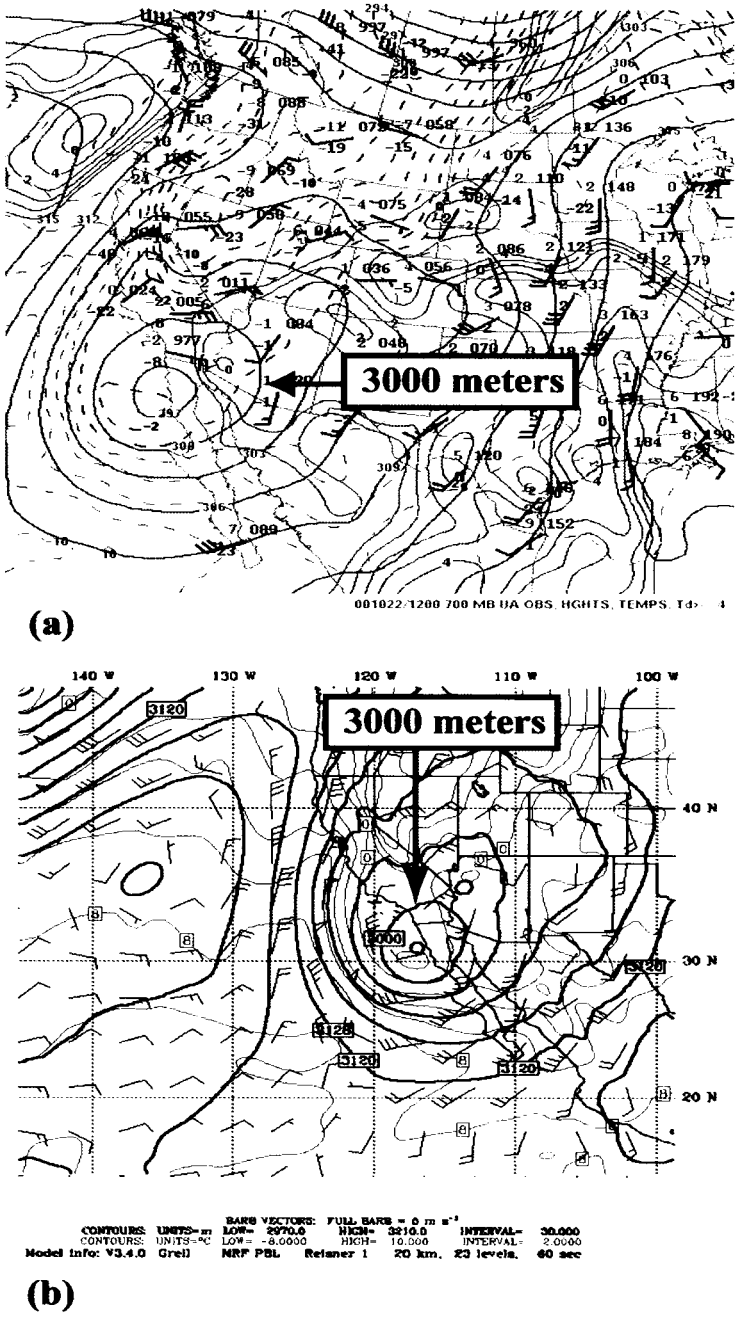

Fig. 25. Same as Fig. 24, but for 700 mb.

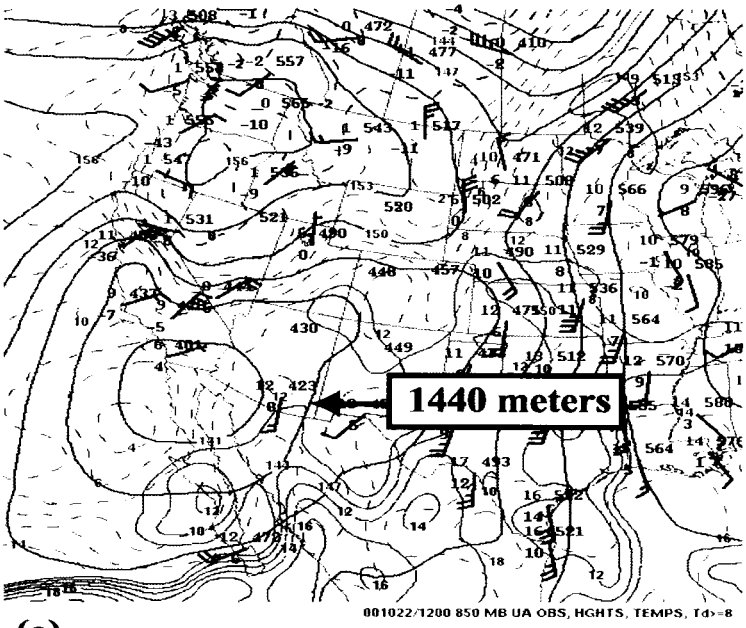

(a)

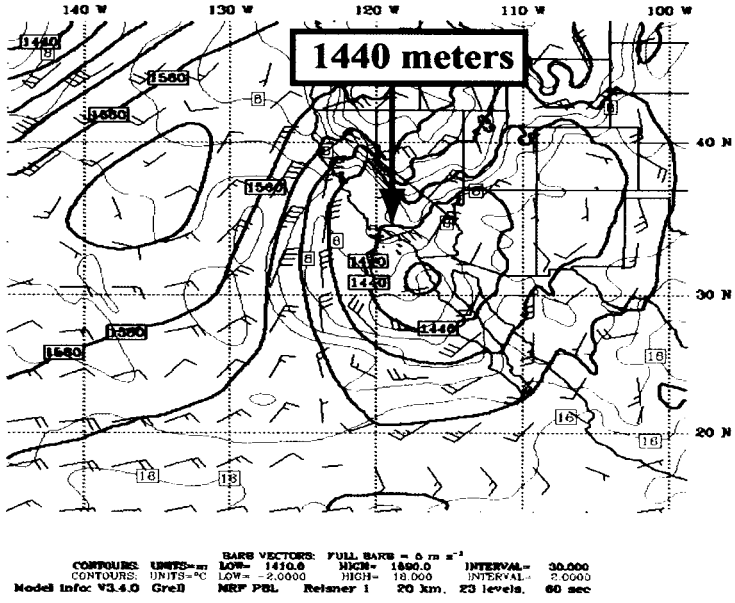

(b)

Fig. 26. Same as Fig. 25, but for 850 mb.

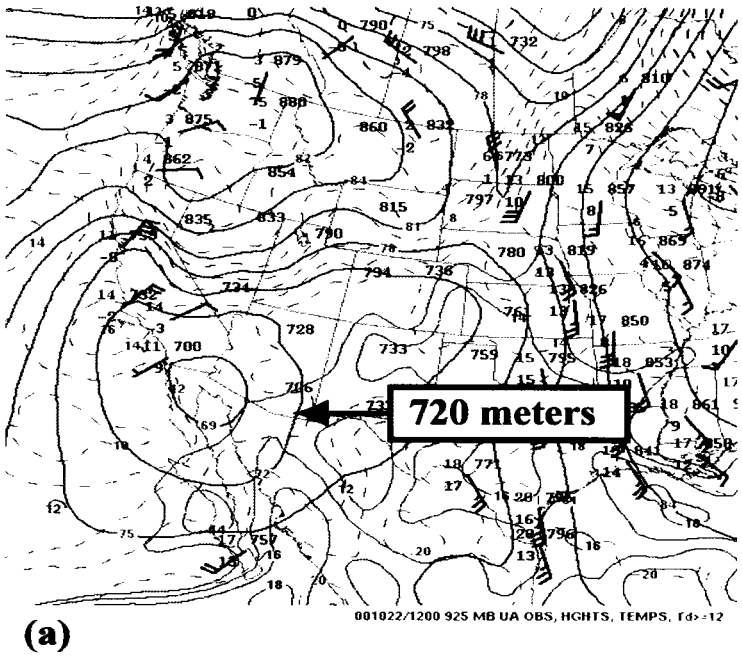

(a)

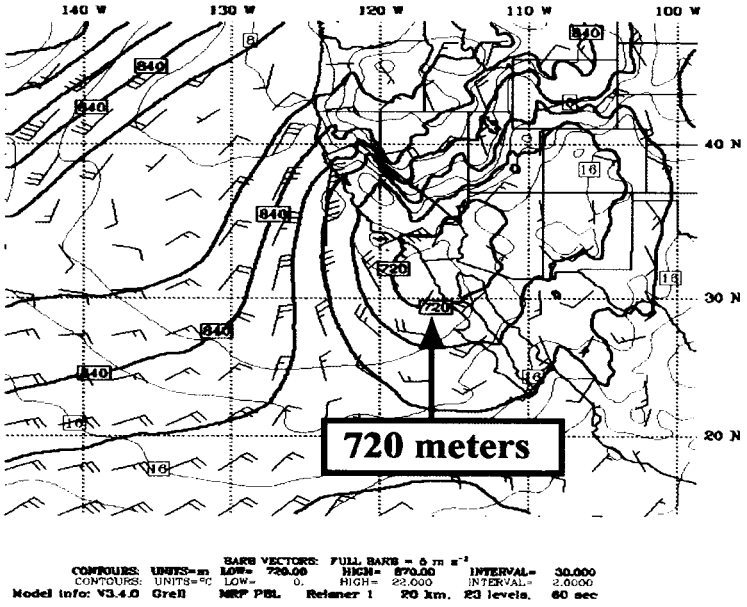

(b)

Fig. 27. Same as Fig. 26, but for 925 mb.

To evaluate MM5 vertical profiles, 12-h forecasts of temperature and moisture were compared to RAOB data from Forecast Systems Laboratory (FSL) for 22 October 2000 at 1200 UTC for 15 western sites within the simulation domain (Fig. 28). MM5 data were interpolated to RAOB pressure levels by use of bilinear vertical interpolation in *ln(p)* and a nearest neighbor technique in the horizontal. MM5 dewpoint temperature was derived from its 3-D relative humidity (RH) and temperature values.

Fig. 28. RAOB sites used for vertical temperature and moisture verification.

For temperature (Fig. 29), MM5 shows excellent agreement with observations, with a maximum domain averaged root mean square error (RMSE) of 8.0 K at 300 mb (Fig 30). At almost all locations however, MM5 fails to resolve a region of warmer air below 300 mb, which results from a MM5 under-prediction of subsidence. Dewpoint temperature profiles also agree well with observations, with a maximum domain averaged RMSE of 9.5 K at 850 mb (Fig. 31). The large 850 mb RMSE is due primarily to its failure to resolve dry air observed at OAK and VBG, both in the subsidence region

behind the front. Both of these errors could have resulted from poorly resolved topography with the relatively coarse (20 km) resolution.

To obtain a good comparison between simulated and observed radiance values, vertical profiles of moisture and temperature must first compare well (as shown above). For a standard mid latitude atmosphere, a temperature difference of 10 K over a 50 mb vertical interval resulted in only a 0.2 % difference in radiance integrated over the 10.7 to 10.9 μm bandwidth, while the difference between a clear mid-latitude and a clear tropical profile produced a 30% difference. That MM5 correctly simulated the synoptic pattern and atmospheric vertical structure for this region was encouraging.

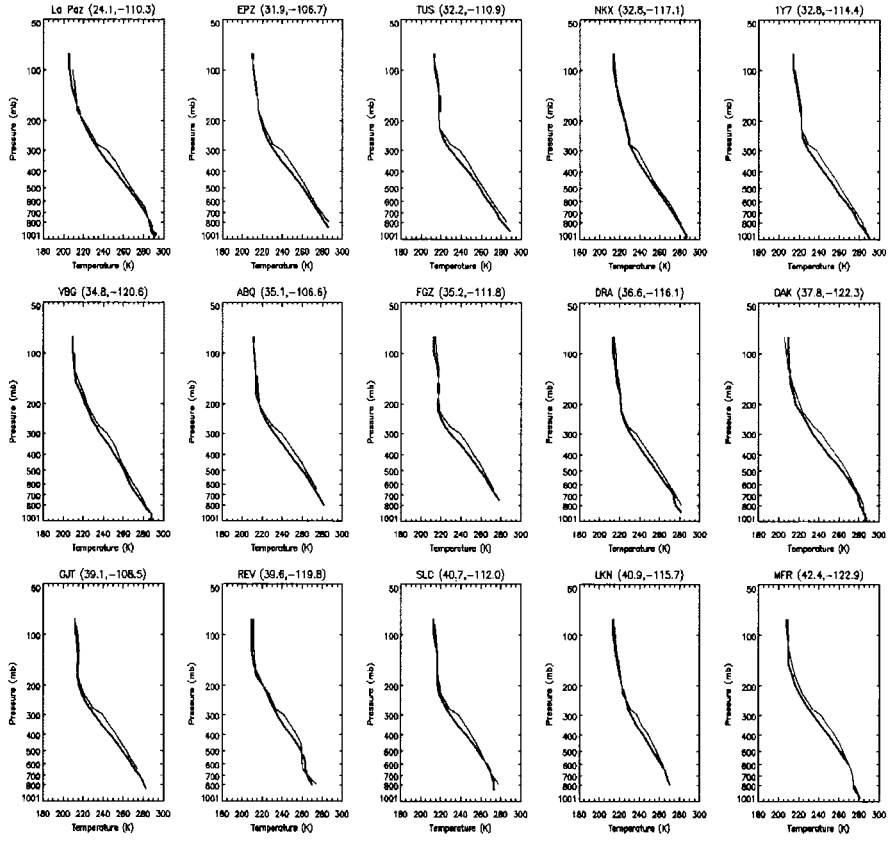

Fig. 29. Observed RAOB (red) and simulated MM5 (blue) temperature (K) profiles.

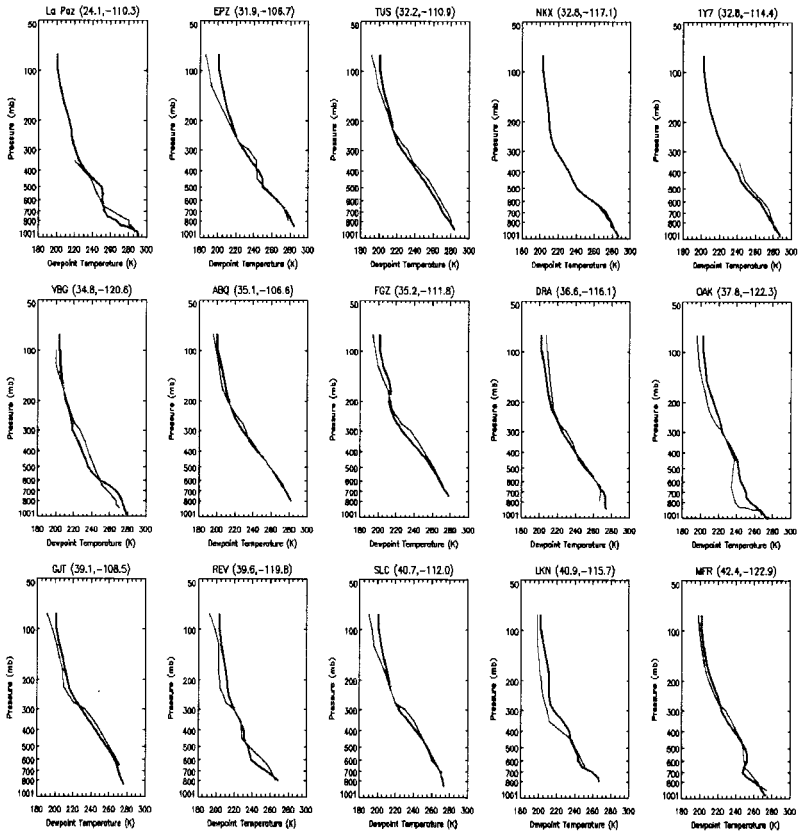

Fig. 30. Same as Fig. 29 but for dewpoint temperature.

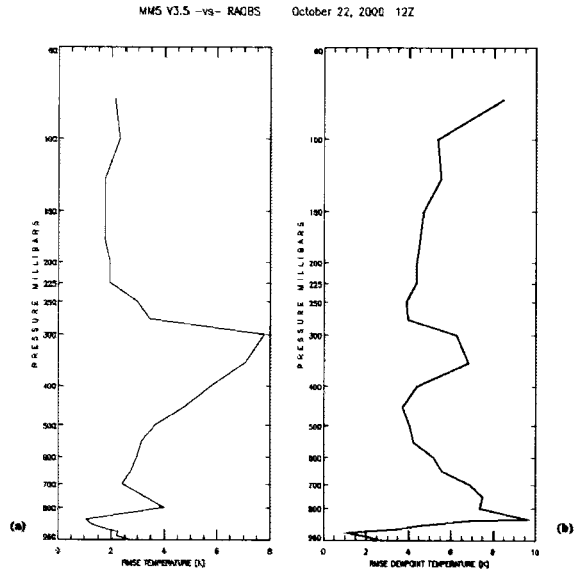

Fig. 31. Domain averaged RMSE (K) for (a) temperature and (b) dewpoint temperature.

To evaluate forecasted MM5 cloud positions, a cloud mask was derived from its cloud liquid water and cloud ice values and then compared to the MODIS cloud mask EDR. A cloud mask is a binary product, in which a value of 1 is cloud and a 0 is clear. To derive the MM5 cloud mask, 3-D cloud liquid water and cloud ice mixing ratios were first column integrated, and added together to produce 2-D gridded fields of cloud water and ice, and then interpolated to the MODIS grid by use of a cubic spline. A threshold of 0.002 g kg^{-1} is used to determine cloud presence.

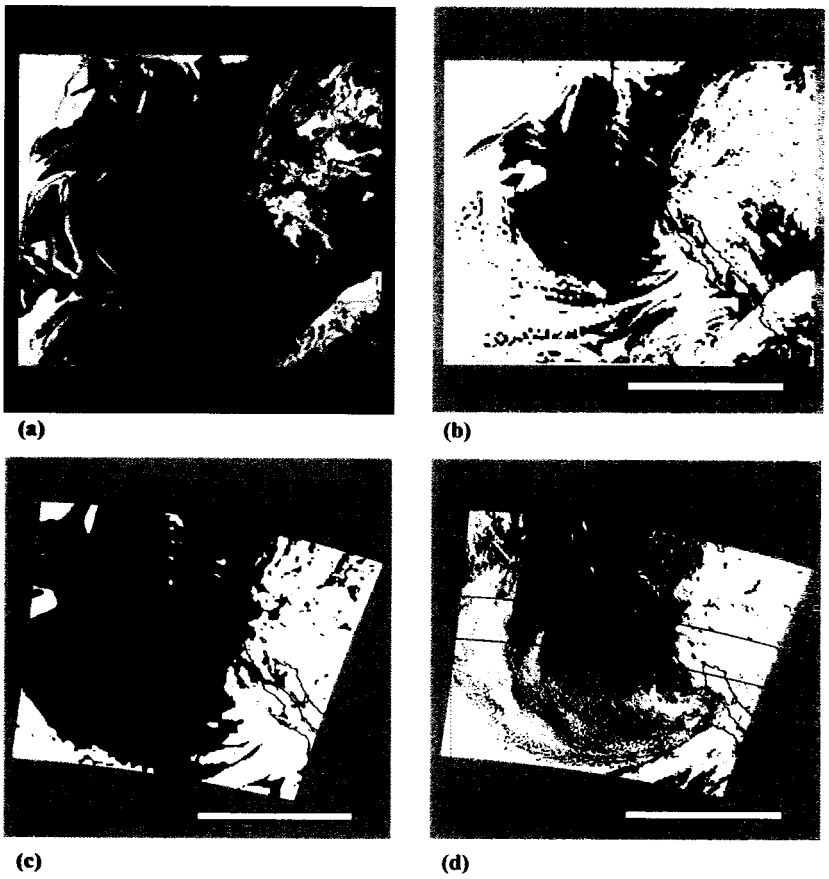

Fig. 32. MM5 cloud: (a) ice mixing ratio (white), water mixing ratio (light blue), rain water mixing ratio (dark blue), and 500 mb wind barbs (red), (b) cloud mask derived from cloud liquid water and cloud ice mixing ratios. MM5 cloud mask (c) interpolated to MODIS 1 km grid and observed MODIS (d) cloud mask EDR.

MM5 forecast of horizontal cloud positions on 22 October at 1900 UTC agree well with observed MODIS satellite data (Fig. 32). Since MM5 was run on a 20 km horizontal-resolution grid, observed small cumulus features over the oceans and terrain cannot be captured, but the position of the cold front that extends SW from the southern Baja coast was simulated particularly well.

Verification of the NOAH-LSM was performed by use of MODIS LST and SST data and from soil temperature data for 22 October at 1900 UTC from the Arizona Meteorological Network (AZMET). The network contains automated weather stations in both urban and rural areas throughout Arizona. The current study uses its air (2 m) and soil (0.1 and 0.5 m) temperatures.

MM5 values were first interpolated to the AZMET sites by use of a cubic spline, and then four comparisons were made between the 19-hr forecast values on 22 October at 1900 UTC and the AZMET data. Three comparisons involved soil temperature: AZMET 0.1 versus MM5 0.1 m, AZMET 0.1 versus MM5 0.3 m, and AZMET 0.5 versus MM5 0.3 m; the fourth was AZMET 2 m versus MM5 2 m air temperatures.

Comparisons between MM5 0.3 and 0.1 m soil temperatures versus AZMET 0.1 m data produced RMSE values of 6.2 K and 5.0 K, respectively. The MM5 LSM 0.3 m versus AZMET 0.5 m soil temperatures produced a RMSE of only 2.2 K, while the 2 m air temperature comparison yielded an even better value of only 1.4 K. The results of the comparisons (biases) are shown in Figs. (33) – (36), where in all cases a positive value indicates that MM5 under predicted temperature.

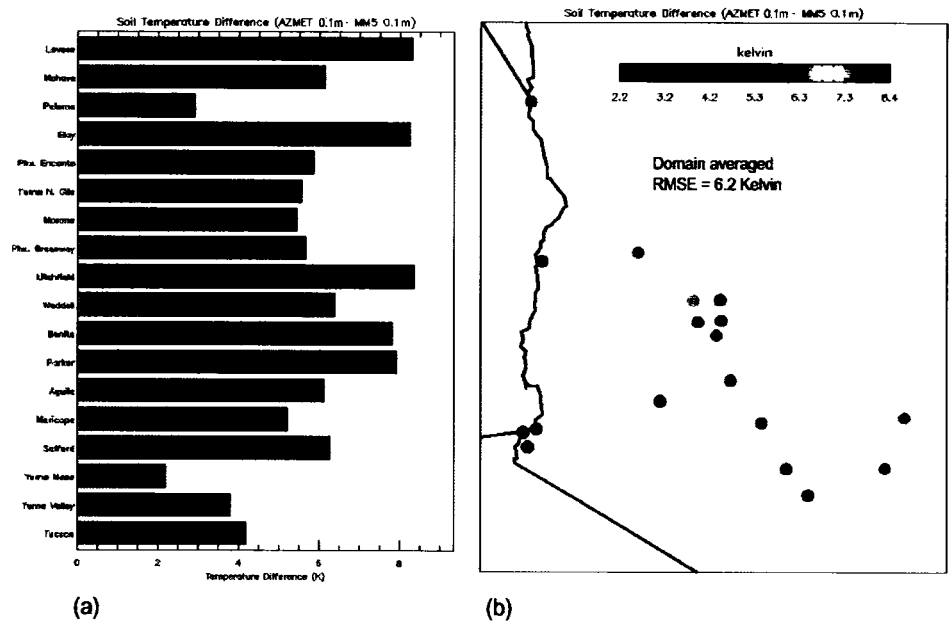

Fig. 33. Calculated: (a) bias and (b) spatial distribution of differences between 0.1 m AZMET and MM5 NOAH-LSM soil temperatures (K).

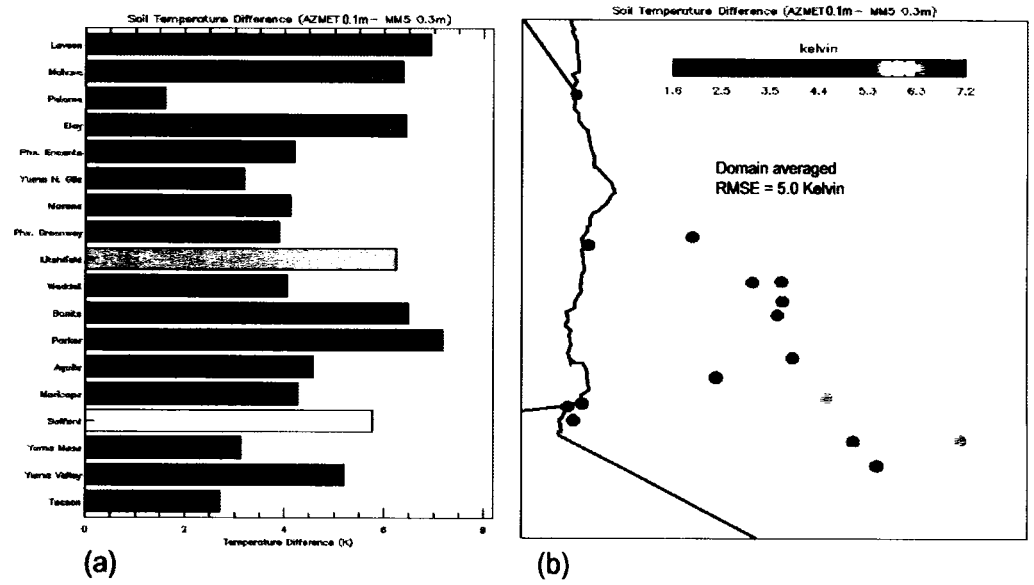

Fig. 34. Calculated: (a) bias and (b) spatial distribution of differences between AZMET measured soil temperature at 0.1 m and MM5 NOAH-LSM simulated soil temperature at 0.3 m in Kelvin.

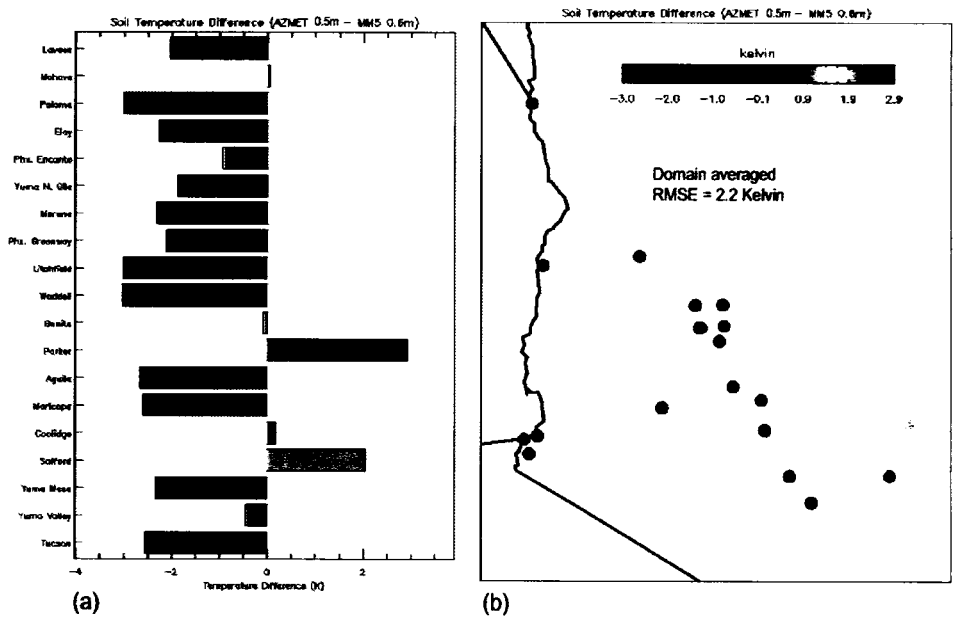

Fig. 35. Calculated: (a) bias and (b) spatial distribution of differences between AZMET measured soil temperature at 0.5 m and MM5 NOAH-LSM simulated soil temperature at 0.6 m in Kelvin.

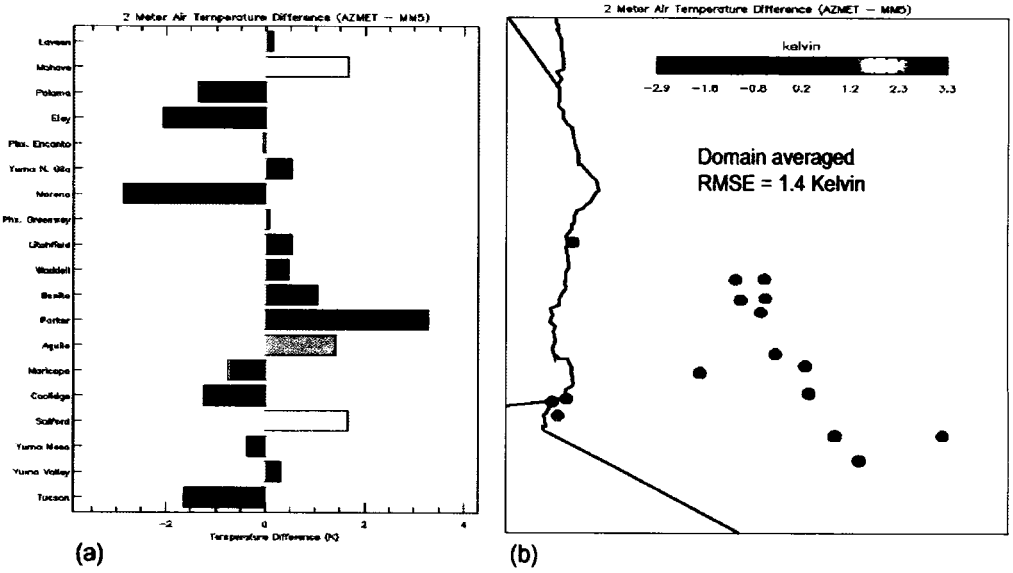

Fig. 36. Calculated: (a) bias and (b) spatial distribution of differences between AZMET measured 2 m air temperature and MM5 simulated 2 m air temperature in Kelvin.

No systematic geographic pattern is evident in any distribution of differences for either soil or air temperatures. Some differences could have resulted as MM5 predicted rain at grid points where no rain had fallen, while others could result from poor instrumentation calibration or from poor initial and boundary conditions in NOAH-LSM. Since soil temperature is not used directly in the TOA radiance simulation, these comparisons are presented primarily for completeness. The 2 m air temperature was, however, used in the TOA radiance simulation, and its 1.5 K domain averaged RMSE had only a negligible effect on the overall results.

Surface temperature verification of NOAH-LSM was performed with MODIS LST and SST EDR data. The SST comparison is presented only for completeness, since NOAH-LSM only predicts land temperatures. As explained in Section 2, MM5 values were first interpolated to a 1 km grid by use of a technique that leveraged the high-resolution land use and terrain data. The interpolated data were then regridded to the MODIS EDR latitude-longitude grid and finally used in direct comparison against MM5 results.

Both the MM5 LST and SST showed a cold bias when compared to the MODIS EDR data (Fig. 37). This is expected for SST data, since the MM5 values are static throughout the integration period, thus the cold upwelled water along the California coast would not captured by MM5. LST differences are expected for several reasons. First MM5 (run here at 20 km) assumes that each grid point is composed of one type of material. The MM5 pre-processing algorithm TERRAIN sets surface type to the most dominate type for each grid point, based on the 1 km USGS material data base. This was par-

tially corrected by the LST and SST post-processing algorithm described in Section 2; however, even at 1 km resolution, the USGS data set has the same artifact. Furthermore, the MM5 radiation scheme treats each grid point as either clear or cloudy, and thus does not account for partial cloudy skies.

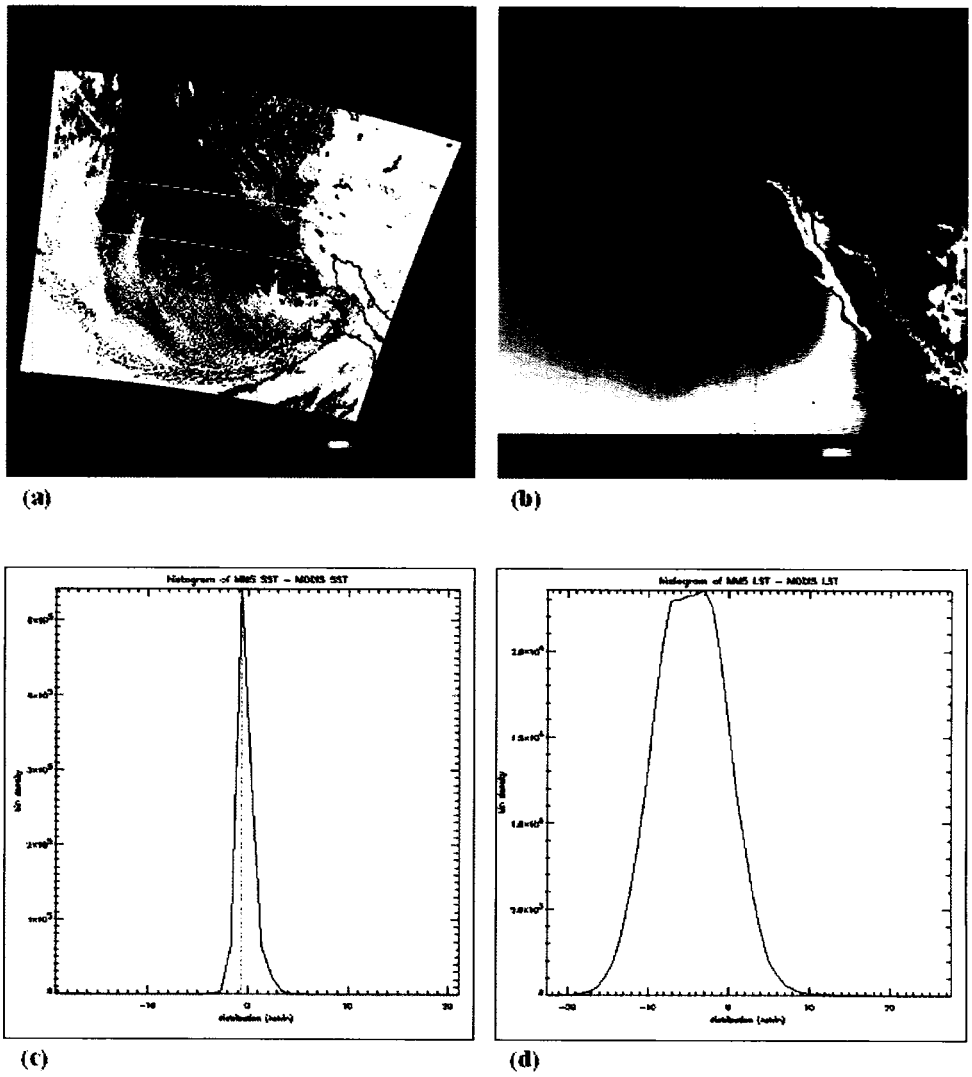

Fig. 37. MODIS LST and SST (K) (a) with cloud mask applied and (b) interpolated 1 km MM5 results, and histograms of (c) MM5 minus MODIS SST and (d) MM5 minus MODIS LST.

Impact from surface temperature errors on resulting the TOA radiance simulation could be significant in the thermal IR bands for materials with high emissivities. Using MODTRAN for a standard clear atmosphere and surface emissivity of 0.5, a change in surface temperature from 300 to 302 K yielded an integrated TOA radiance difference of 3% at nadir for a bandwidth of 10.7 to 10.9 μm. Some errors could also exist in the MODIS LST EDR data as compared to well-calibrated ground truth. Future studies could input MODIS SST and LST data into the MM5 initial conditions to evaluate effects on MM5 results from the cold water and strong SST gradients along the California coast and from accurate LST data.

Comparison between accumulated 3-h precipitation from the MM5 12-h forecast with observed NEXRAD values for 1200 UTC on October 22 was made to evaluate the accuracy of MM5 cloud physics and precipitation values. NEXRAD numerical data files were not available at the time of this study, so the comparison was made qualitatively (Fig. 38). The maximum observed 3-h dBZ is approximately 45 to 50, which converts to 1.2 inches (30 mm) of rain, while the 12-h MM5 forecast produces a maximum of 24 mm. While the MM5 and radar distributions and concentrations are in general agreement, the MM5 precipitation appears primarily topographically induced, while the observed is more wide spread. As radar observations are composite-reflectivity, the actual precipitation reaching the ground may be at the higher elevations.

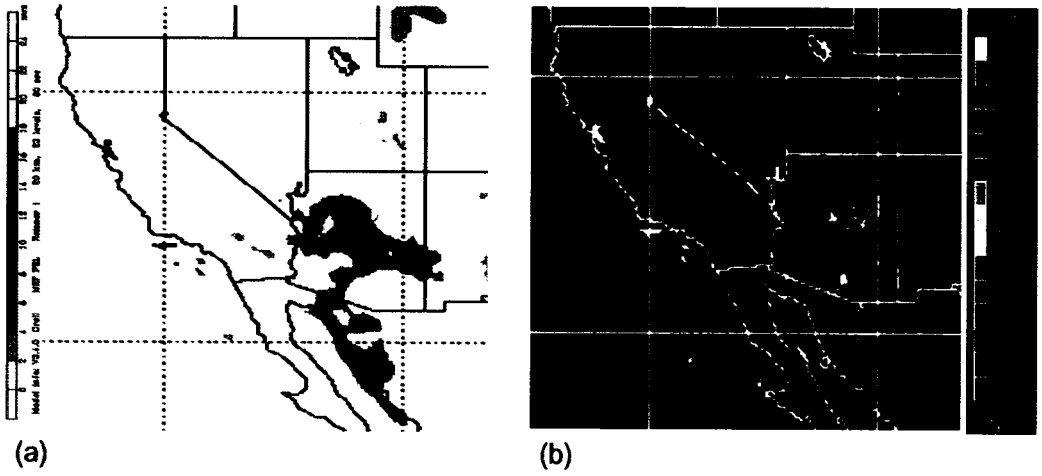

Fig. 38. Three-hour accumulated precipitation for 1900 UTC on 22 October 2000, where (a) is simulated MM5 convective + non-convective (mm) and (b) is NEXRAD composite reflectivity (dBZ).

The MM5 simulation thus agreed well with the observations, as its synoptic pattern and horizontal cloud-distribution compared well with both the Eta analysis and satellite imagery. While the vertical structure of temperature and moisture also compared well with RAOB observations, some noticeable differences in soil temperature exist in the comparison to the AZMET observations.

b. VIIRS simulation results

Output from the VIIRS sensor simulation consisted of 16 bands of digital counts, calibration data, and geolocation data (e.g., latitude, longitude, and time). Digital counts produced by the ARSS MSI modeling system were calibrated to sensor data records (SDR) to produce albedo values and brightness temperatures. SDR values from both VIIRS and MODIS were used in the comparison.

VIIRS data were first interpolated to the MODIS latitude-longitude grid and then two comparisons made. The first compared clear pixels only, with the requirement that the pixels had to be clear in both scenes. The second compared scenes for both clear and cloudy pixels. Table 2 summarizes the bands used in the comparison and the relationship between the VIIRS and MODIS bands. In all cases, VIIRS data were subtracted from MODIS data.

VIIRS Band	Band Width (μm)	Band Center (μm)	MODIS Band	Band Width (μm)	Band Center (μm)
M7	0.846 - 0.885	0.865	2	0.841 - 0.876	0.858
M12	3.610 - 3.790	3.780	20	3.660 - 3.840	3.750
M9	1.371 - 1.386	1.378	26	1.360 - 1.390	1.375
M14	8.400 - 8.700	8.500	29	8.400 - 8.700	8.550
M15	10.263 - 11.263	10.760	31	10.780 - 11.280	11.030
M16	11.966 - 12.916	12.010	32	11.770 - 12.270	12.020

Table 2. Summary of MODIS and VIIRS bands used in TOA comparison.

Results are shown for each comparison in Figs. (39)–(44), where each figure shows: (a) observed MODIS data for 22 October at 1922 UTC, (b) simulated VIIRS data for 22 October at 1900 UTC, (c) a difference image for both clear and cloudy pixels, (d) a histogram of differences for all pixels, (e) difference image for clear pixels only, and (f) histogram of differences for clear pixels. Statistics for each comparison are shown in Table 3.

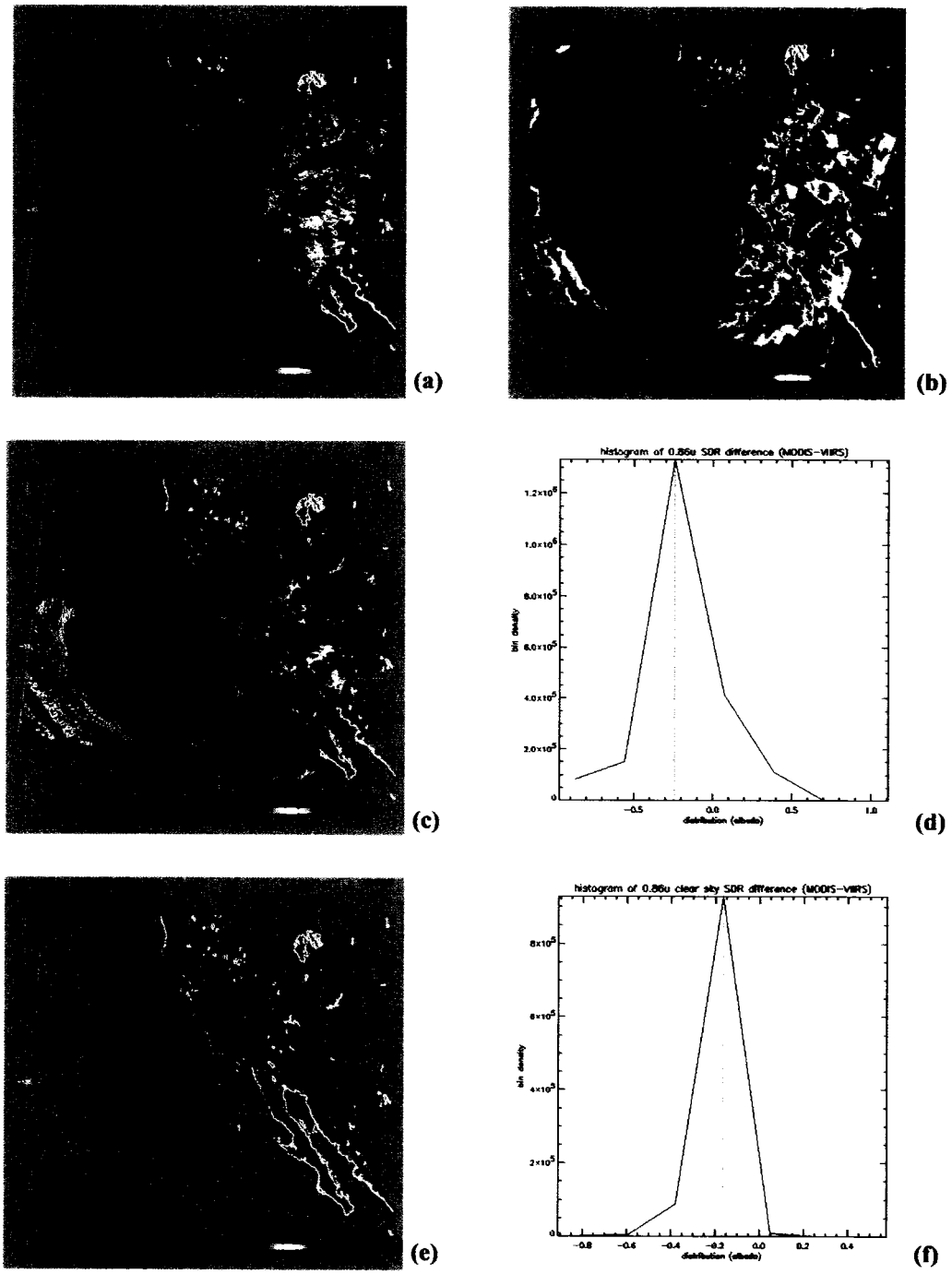

Fig. 39. Comparison of (a) observed MODIS and (b) simulated VIIRS 0.86 μm imagery for (c and d) clear and cloudy pixels and for (e and f) clear pixels only.

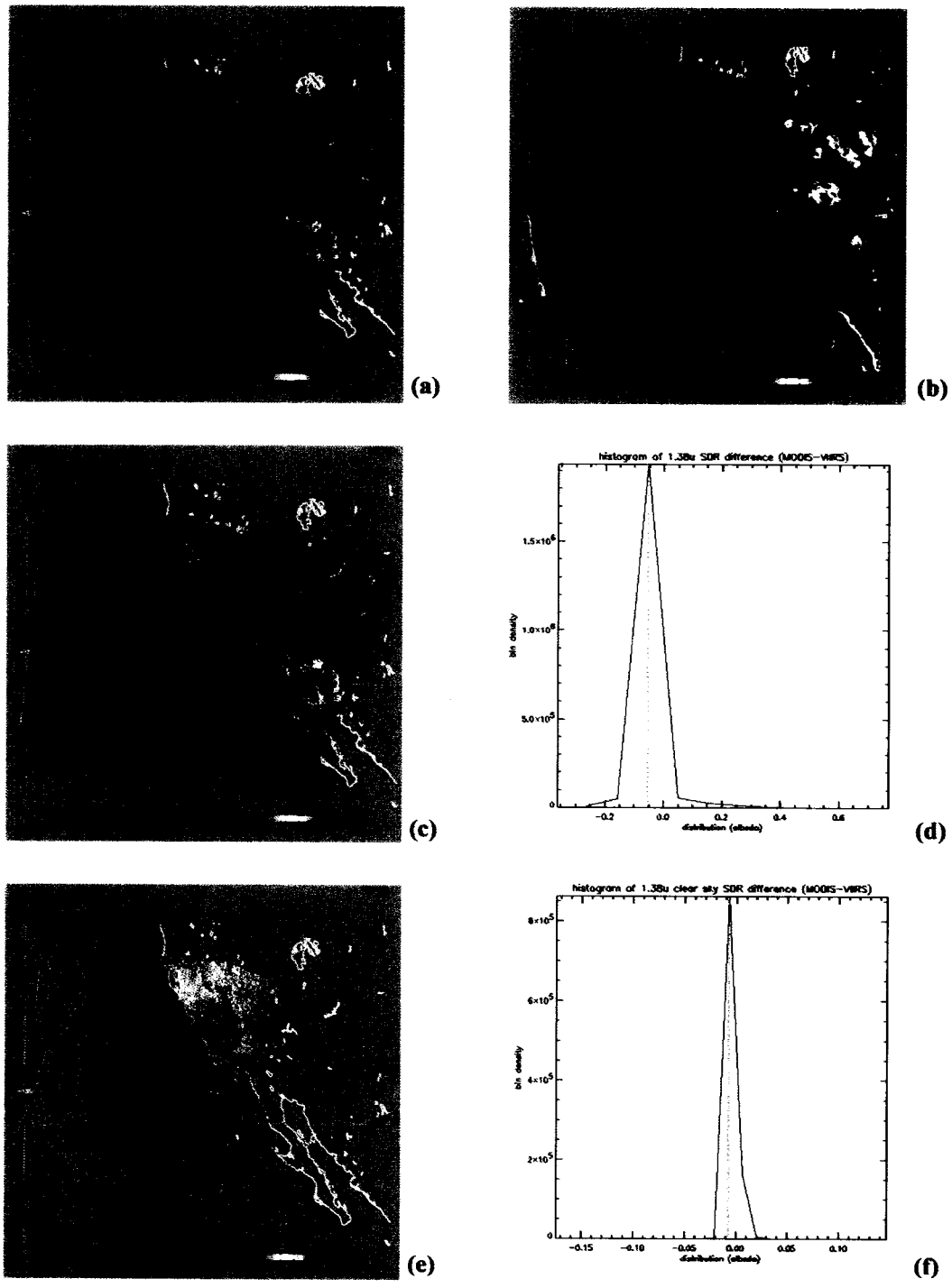

Fig. 40. Same as Fig. 39, but for 1.38 μm.

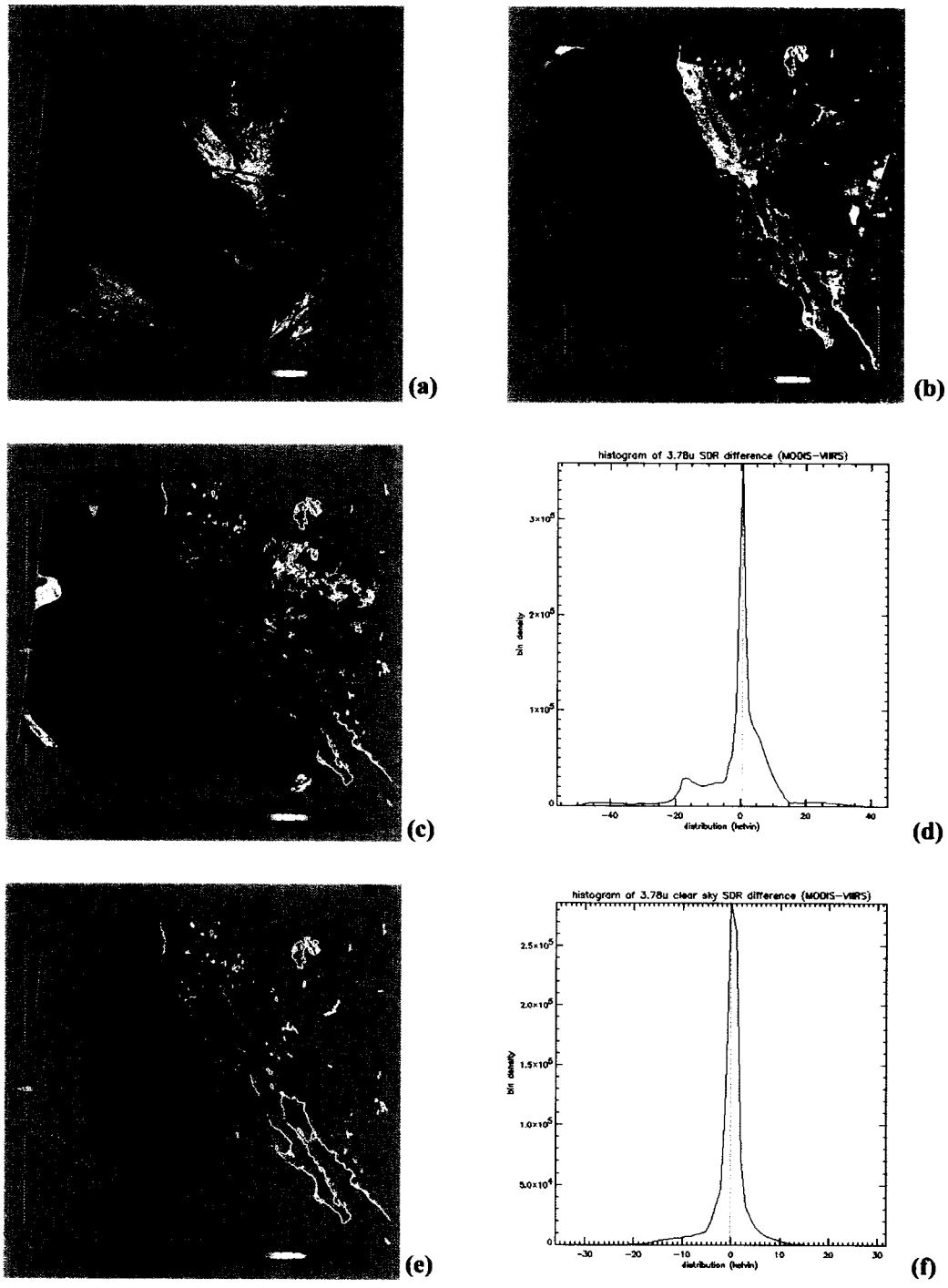

Fig. 41. Same as Fig. 40, but for 3.8 μm.

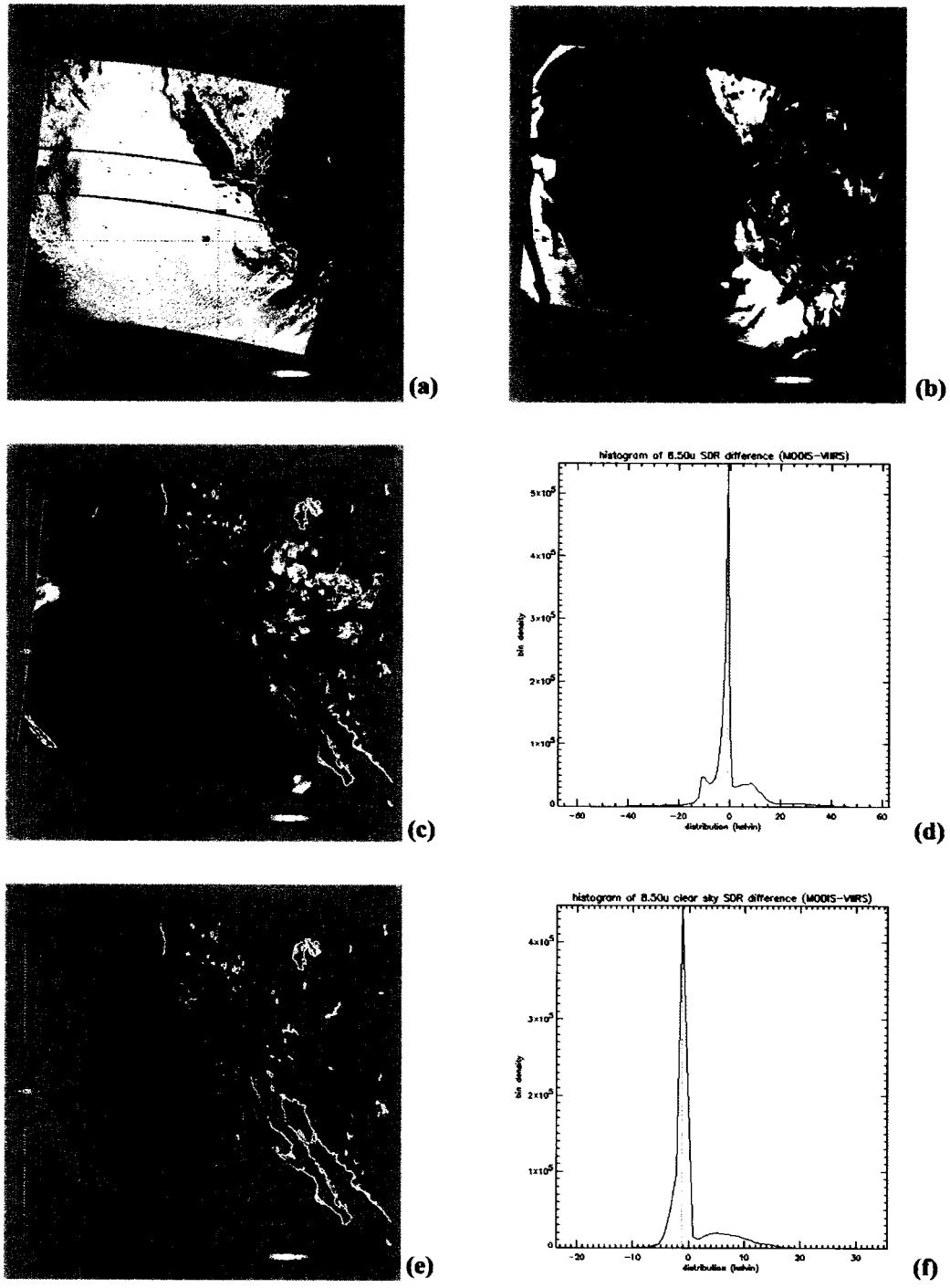

Fig. 42. Same as Fig. 41, but for 8.5 μm.

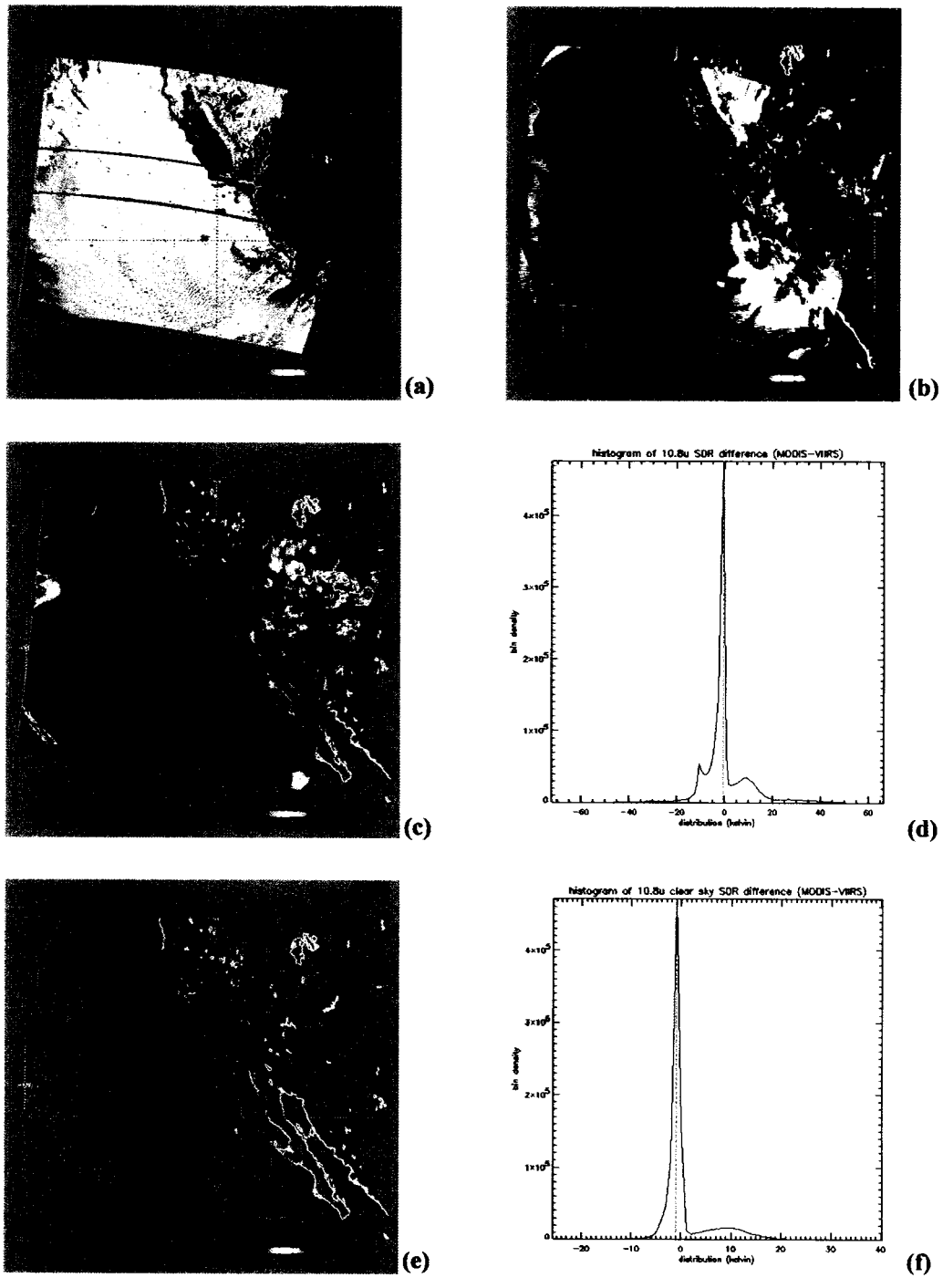

Fig. 43. Same as Fig. 42, but or 10.8 μm.

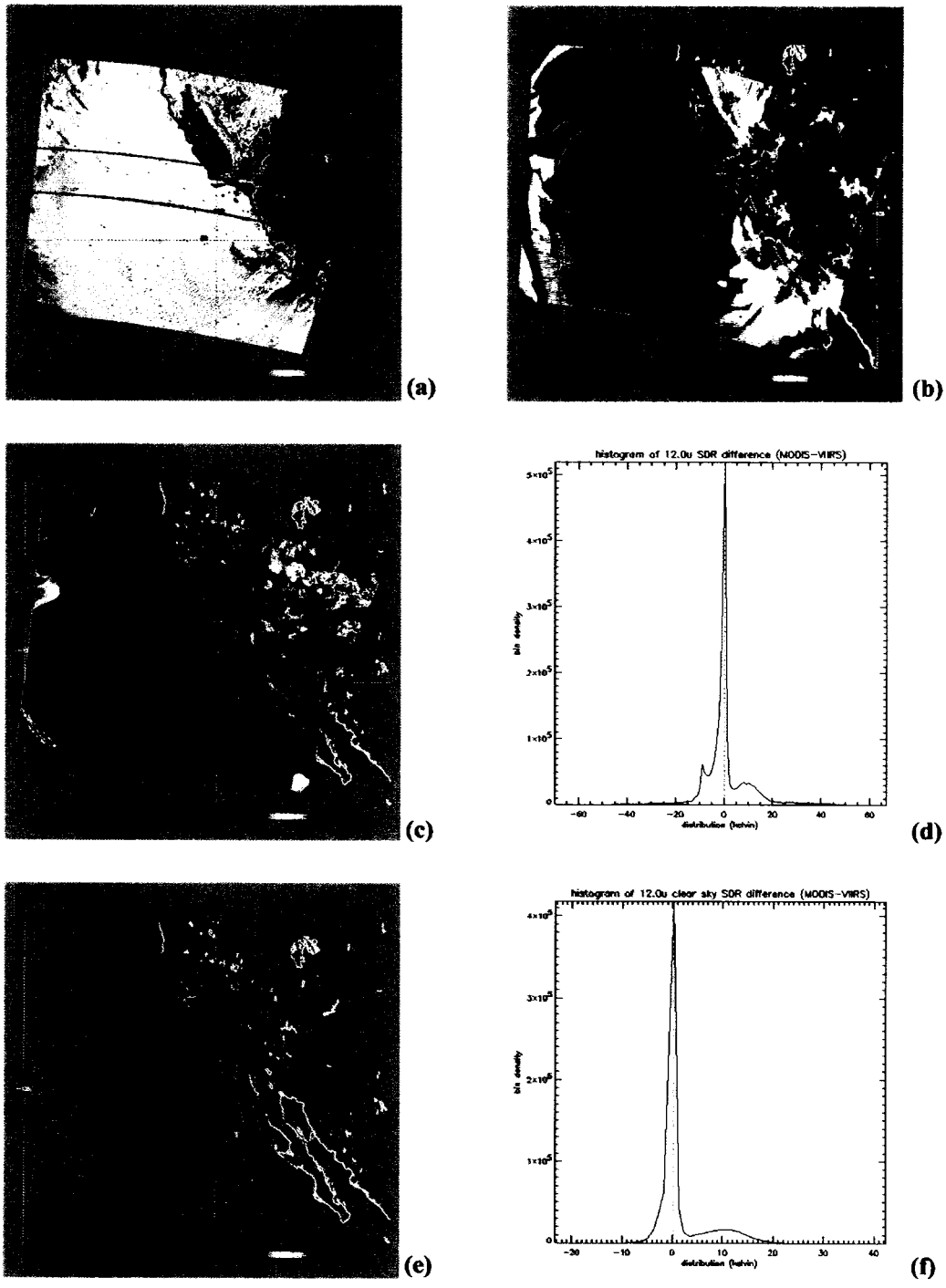

Fig. 44. Same as Fig. 43, but for 12.01 μm.

VIIRS Band Center (μm)	MODIS Band Center (μm)	Figure Number	Clear Sky RMSE	Clear Sky Bias	Cloudy Sky RMSE	Cloudy Sky Bias	Units
0.865	0.858	39	0.097	-0.029	0.233	-0.001	None
1.378	1.375	40	0.005	0.003	0.051	0.009	None
3.780	3.750	41	3.700	0.200	10.510	-0.496	K
8.500	8.550	42	3.910	0.739	9.941	0.610	K
10.760	11.030	43	4.694	1.137	10.678	0.571	K
12.010	12.020	44	5.094	2.019	10.641	1.281	K

Table 3. Summary of results of comparison between simulated VIIRS and observed MODIS values.

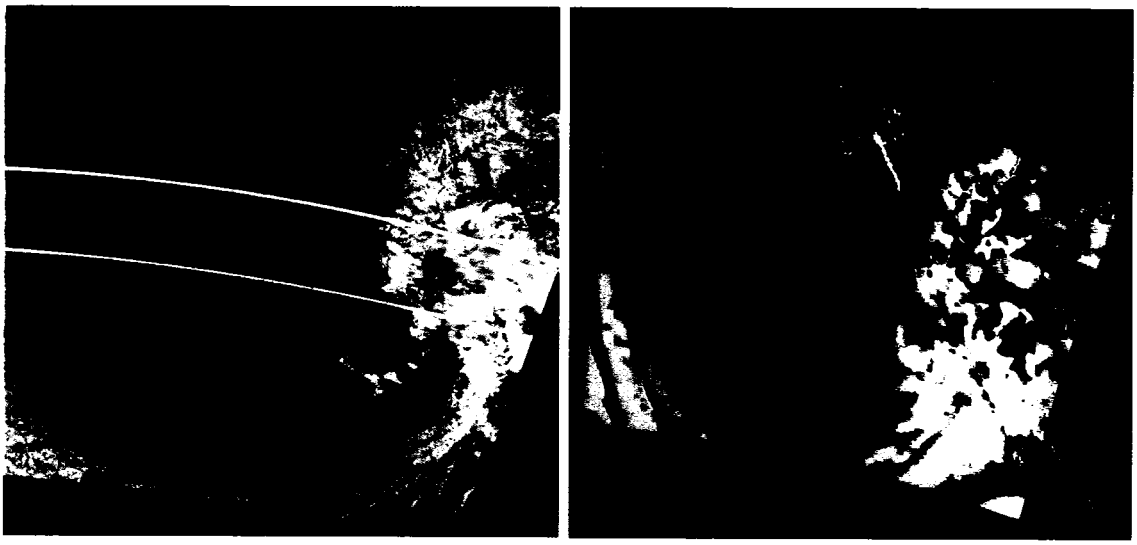

Fig. 45. Composite images from: (a) MODIS RGB observations from bands 1, 2, and 31 (inverted) and (b) simulated VIIRS RGB from bands M1, M7, and M15.

4. Conclusion

A scene simulation system that uses MM5 and MODTRAN has been developed to estimate TOA radiance values based on non-homogeneous atmospheric radiative transport calculations. Linkage between these two models provides accurate 3-D numerical simulations of the atmosphere coupled with a state of the art radiative transfer model. The study focused on the simulation of VIIRS E-O sensor data to support development of EDR algorithms for the NPOESS satellite. The end-to-end simulation can be summarized as follows:

1. Acquire EOS MODIS Level 1B, geolocation, and EDR data for 22 October 2000 at 1922 UTC
2. Acquire meteorological observations and large scale model output
3. Use MM5 to simulate mesoscale atmospheric quantities coincident with MODIS data
4. Post-process MM5 data and generate a GDC
5. Use the MODTRAN based ARSS to simulate TOA radiance values for the VIIRS sensor by use of input GDC data
6. Calibrate VIIRS RDR data to SDRs
7. Compare observed MODIS data to simulated VIIRS data.

Considering the complexity of the effort, VIIRS simulated values compare remarkably well to observed MODIS data. While the system is computationally intensive, the results demonstrate that it effectively models most first-level phenomenology (i.e.,

diffuse reflectance, passive thermal variation, atmospheric transmission, and path radiance) for extended complex scenes.

Using a fairly straightforward setup (e.g. no observation nudging, no nesting), MM5 effectively modeled self-consistent surface and atmospheric state parameters for use in subsequent radiative transfer modeling. The model accurately captured the synoptic and mesoscale features of the atmosphere on 22 October 2000 at 1900 UTC and compared well to observations. The TOA radiance modeling also compared well to observations in the visible, near-, mid- and, long-wave infrared régimes, as shown by the direct comparison between simulated and observed brightness temperatures.

Some differences with observations do exist, however, and those can be partly attributed to the modeling system. Results would have been even better in a pure clear-sky comparison if multiple MODTRAN runs would have been executed on every pixel, rather than just for MetCell centers. Errors also resulted from: imperfect atmospheric state-variables produced by MM5, use of climatological atmospheric quantities above the MM5 domain, lack of atmospheric aerosol knowledge, errors in the USGS surface emissivities, and pixel adjacency effects. Other error sources include inaccurate modeling of radiative transfer phenomena, such as BRDF effects and from multiple scattering effects in both clear and cloudy atmospheres.

Some larger differences (especially in cloudy pixels) can be explained by errors in predicted cloud position, e.g., if a MM5 cloud was computed at a vertical or horizontal position not observed, simulated VIIRS products could have a 20 to 30 K temperature difference, as compared to those observed by MODIS.

Future efforts could include the modeling of multiple cloud layers, instead of just the two used for this study and the coupling of MM5 output to an upper-atmosphere numerical model to obtain more accurate values above the MM5 domain.

References

Anderson, G. P., F. X. Kneizys, J. H. Chetwynd, J. Wang, M. Hoke, L. S. Rothman, L. M. Kimball, R. McClatchey, E. P. Shettle, S. A. Clough, W. O. Gallery, L. Abreu, and J. Selby, 1995: FASCODE/MODTRAN/LOWTRAN: Past/Present/Future, 18th Annual Review Conf. on Atmospheric Transmission Models proceeding, 6-8 June, 16 pp.

Arakawa, A., and V. Lamb, 1977: Computational Design of the Basic Dynamical Processes of the UCLA General Circulation Model, *Methods in Computational Physics*, **17**, 174-267.

Berk, A., Bernstein, L. S., Robertson, 1989: MODTRAN: a moderate resolution model for LOWTRAN 7, GL-TR-89-0122, Spectral Sciences, Burlington, MA, 27 pp.

Berk, A., G. P. Anderson, and B. Gossage, 2001: MOD3D: A model for incorporating MODTRAN radiative transfer into 3D simulations, SPIE proceeding, algorithms for multispectral, hyperspectral and ultraspectral imagery I/II, **4381**, 470-476.

Bluestein, H. B., 1992: *Synoptic-Dynamic Meteorology in Midlatitudes Vol-1*. Oxford Press, NY, 421 pp.

Bryan, G. H., and J. M. Fritsch, 2003: Are the Sub-grid Mixing Schemes in MM5 Adequate for Cloud-Scale Simulations?, MM5 Community Workshop, 56-59.

Cipperly, G. E., and S. A. Wilcox, 1999: PACEOS IIa Users Manual, Lockheed Martin Technical Memorandum, 17 pp.

Chen, F., and J. Dudhia 2001: Coupling an advanced land surface-hydrology model with the Penn State-NCAR MM5 modeling system. Part I: model implementation and sensitivity. *Mon. Wea. Rev.*, **129**, 569-585.

Cipperly, G. E., 2002: Entrance Aperture Radiance Modeling for Multi-Spectral Sensor Simulations, Lockheed Martin Technical Memorandum, 62 pp.

DIRS, 2004: The DIRSIG Users Manual, Digital Image and Remote Sensing Laboratory, Rochester Institute of Technology, 298 pp.

Dudhia, J., 1989: Numerical study of convection observed during the winter monsoon experiment using a mesoscale two-dimensional model. *J. Atmos. Sci.*, **46,** 3077-3107.

Dudhia, J., 1993: A nonhydrostatic version of the Penn State/NCAR mesoscale model: Validation tests and simulation of an Atlantic cyclone and clod front. *Mon. Wea. Rev.*, **121**, 1493-1513

Dudhia, J., and J. Bresch 2002: A Global Version of the Penn State-NCAR Mesoscale Model., *Mon. Wea. Rev.*, **130**, 2989-3007.

Dudhia, J., D. Gill, Y-R., Guo, D. Hansen, K. Manning, and W. Wang, 1999: PSU/ NCAR Mesoscale Modeling System Tutorial Class Notes and Users' Guide: MM5 Modeling System Version 3. Mesoscale and Microscale Meteorology Division, NCAR, 182 pp.

Dyer, A. J., 1974: A review of flux-profile relationships, *Bound.Layer Meteor.*, **7**, 363-372.

Grell, G., J. Dudhia, and D. Stauffer, 1995: A Description of the Fifth-Generation Penn State/NCAR Mesoscale Model (MM5). Mesoscale and Microscale Meteorology Division, NCAR/TN-398+STR, 117 pp.

Grell, G. A., Y. H. Kuo, and R. Pasch, 1991: Semi-prognostic tests of cumulus parameterization schemes in the middle latitudes. *Mon. Wea. Rev.*, **119**, 5-31.

Guo, Y-R., and S. Chen, 1994: Terrain and Land Use for the Fifth-Generation Penn State/ NCAR Mesoscale Modeling System (MM5). Mesoscale and Microscale Meteorology Division, NCAR/TN-397+IA, 115 pp.

Haltiner, G. J., and R. Williams, 1980: *Numerical Prediction and Dynamic Meteorology*. John Wiley and Sons, NY, 477 pp.

Hicks, B. B., 1976: Wind profile relationships from the `Wangara' experiments, *Quart. J. Roy. Meteor. Soc.*, **102**, 535-551.

Holton, J. R., 1992: *An Introduction to Dynamic Meteorology*. Academic Press, NY, 511 pp.

Kennedy, P. J., and M. A. Shapiro, 1980: Further encounters with clear air turbulence in research aircraft. *J. Atmos. Sci.*, **37**, 986-993.

Kidder, S. Q., and T. Vonder Haar, 1995: *Satellite Meteorolog, an Introduction*. Acdemic Press, NY, 466 pp.

Kim, J., and L. Mahrt, 1992: Turbulent mixing in the stable free atmosphere and the nocturnal boundary layer. *Tellus*, **44a**, 381-394.

Mahrt, L., and M. Ek, 1984: The influence of atmospheric stability on potential evaporation. *J. Clim. Appl. Meteorol.*, **23**, 222-234.

McClatchey, R., R. W. Fenn, J. E. A. Selby, F. E. Volz, and J. S. Garing, 1972: Optical Properties of the Atmosphere (3rd Edition), AFCRL-72-0497 (NTIS AD A753075), 217 pp.

McClatchey, R. A., R. W. Fenn, J. E. A. Selby, F. E. Volz, and J. Garing, 1970: Optical Properties of the Atmosphere, AFCRL-70-0527, (AD A715270), 209 pp.

Pielke, R. A., 2002: *Mesoscale Meteorological Modeling.* International Geophysical Series, NY, 676 pp.

Posselt, D. J., E. R. Olson, and J. A. Otkin, 2003: Use of high resolution MM5 simulations for gifts forward model and retrieval algorithm development, MM5 Community Workshop, 56-59.

Reisner, J., R. J. Rasmussen, and R. T. Bruintjes, 1998: Explicit forecasting of supercooled liquid water in winter storms using the MM5 mesoscale model. *Quart. J. Roy. Meteor. Soc.*, **124B**, 1071-1107.

Richtsmeier S. C., A. Berk, L. S. Bernstein, and S. M. Adler-Golden, 2001: *A 3-dimensional radiative-transfer hyperspectral image simulator for algorithm validation*, International Symposium on Spectral Remote Sensing, 9 pp.

Schott, J. R., 1997: *Remote Sensing, The Image Chain Approach.* Oxford University Press, NY, 394 pp.

Schott, J. R., R. Raqueno, and C. Salvagio, 1992: Incorporation of time-dependent thermodynamic model and radiation propagation model into infrared three-di-mensional synthetic image generation, *Optical engineering*, **31**, 1505-1516.

Selby, J. E. A, and R. A. McClatchey, 1972: Atmospheric Transmittance from 0.25 to 28.5 m: Computer Code LOWTRAN 2, AFCRL-TR-72-0745, AD A763721, 44 pp.

Shir, C. C., and R. D. Bornstein, 1977: Eddy exchange coefficients in models of the PBL. *Boundary Layer Meteor.*, **11**, 171-186.

J. P. Smith, D.J. Dube, M.E. Gardner, S. A. Clough, F.X. Kneizys, and L.S. Rothman, 1978: FASCODE - Fast Atmospheric Signature Code (Spectral Transmittance and Radiance), AFGL-TR-78-0081, Air Force Geophysics Lab., Hanscom AFB, 88 pp.

Smagorinski, J., S. Manabe, and J. L. Holloway, Jr., 1965: Numerical results from a nine-level general circulation model of the atmosphere, *Mon. Wea. Rev.*, **93**, 727-768.

Troen, I., and L. Mahrt, 1986: A simple model of the atmospheric boundary layer: Sensitivity to surface evaporation. *Bound. Layer Meteorol.*, **37**, 129-148.

Wilcox, S. A., and G. E. Cipperly, 1999: PACEOS IIa Users Manual, Lockheed Martin Technical Memorandum, 17 pp.

Appendix A: List of symbols

Symbol	*Meaning*
$()_0$	Reference state variable
$()'$	Perturbation variable
c_v	Specific heat of air at constant volume
c_p	Specific heat of air at constant pressure
g	Gravity
h	Height of planetary boundary layer
k	von Karman constant
m	Map scale factor
p	Average Pressure
p_s	Pressure at surface of model
p_t	Pressure at top of model domain (defined by user)
p^*	Difference between p_s and p_t
$\hat{p}$	Total pressure
p''	Turbulent pressure
q_c	Cloud water and ice
q_r	Rain water and snow
q_v	Water vapor
r	Reflectance

r_{earth}	Radius of earth
t	Time variable
u	x wind components (eastward)
u_*	Friction velocity
v	y wind components (northward)
w	z wind component (upward)
w_s	Mixed layer velocity
Δx	Distance between grid points in x-direction
Δy	Distance between grid-points in y-direction
Δs	Distance between grid points on spherical earth
A	General variable
C	Volumetric heat capacity
D	Deformation
$D_{\theta,x,y,z}$	Molecular diffusion
$E_{d\varepsilon\lambda}$	Atmospheric downwelling irradiance from scattering
$E_{S\lambda}$	Exoatmospheric solar irradiance
F_{sky}	Fraction of hemisphere above pixel that is sky
F_x	Frictional force in x direction
F_y	Frictional force in y direction
F_z	Frictional force in z direction
$F_{H2\alpha}$	Second-order horizontal diffusion

$F_{H4\alpha}$	Fourth-order horizontal diffusion
K	Horizontal eddy diffusivity
L	Monin Obukhov length
$L_{bs\lambda}$	Radiance from background scattering
$L_{b\varepsilon\lambda}$	Radiance from background emission
$L_{us\lambda}$	Upwelling radiance from atmosphere due to scattering
$L_{u\varepsilon\lambda}$	Upwelling radiance from atmosphere due to emission
L_{Sensor}	Total radiance at sensor aperture
$L_{T\lambda}$	Blackbody radiance
P_{CON}	Condensation of water vapor into cloud/ice at saturation
P_{RA}	Accretion of cloud by rain (ice by snow)
P_{RC}	Conversion of cloud to rain (ice to snow)
P_{RE}	Evaporation (sublimation) of rain (snow)
P_{II}	Initiation of ice crystals
P_{ID}	Sublimation/deposition of cloud ice
T	Temperature
T_v	Virtual temperature
Q	Air parcel heat
$\dot{Q}$	Diabatic heating
R_d	Gas constant for dry air
$\vec{\mathbf{V}}$	3-D wind vector

$\vec{V}_H$	2-D horizontal wind vector
X	Cartesian coordinate map-variable in x-direction
Y	Cartesian coordinate map-variable in y-direction
α	Specific volume
γ	Ratio of specific heats
γ_A	Counter-gradient term
ε	Emissivity
θ	Potential temperature
θ_*	Temperature scale
λ	Longitude
ρ	Density
σ	Sigma coordinate variable
σ_{zenith}	Solar zenith angle
τ_1	Atmospheric transmission from sun to target
τ_2	Atmospheric transmission from target to sensor
ϕ	Latitude
ϕ_M	Non-dimensional wind-shear parameter
ϕ_θ	Non-dimensional buoyancy parameter
ω	Vertical velocity in isobaric coordinates
Θ	Volumetric soil-water content
$\vec{\Omega}$	Angular velocity of earth